Wave simulation in heterogeneous transversely isotropic porous media with fractional attenuation: a Cartesian grid approach

Emilie Blanc, Guillaume Chiavassa, Bruno Lombard

Emilie Blanc, Guillaume Chiavassa, Bruno Lombard. Wave simulation in heterogeneous transversely isotropic porous media with fractional attenuation: a Cartesian grid approach. 2014. hal-00949686v1

HAL Id: hal-00949686
https://hal.science/hal-00949686v1

Preprint submitted on 20 Feb 2014 (v1), last revised 4 Jul 2014 (v2)

Wave simulation in heterogeneous transversely isotropic porous media with fractional attenuation: a Cartesian grid approach

Emilie Blanc[a], Guillaume Chiavassa[c,*], Bruno Lombard[b]

[a]Division of Scientific Computing, Department of Information Technology, Uppsala University, P.O. Box 337, SE-75105 Uppsala, Sweden
[b]Laboratoire de Mécanique et d'Acoustique, UPR 7051 CNRS, 31 chemin Joseph Aiguier, 13402 Marseille, France
[c]Centrale Marseille, M2P2, UMR 7340 - CNRS, Aix-Marseille Univ., 13451 Marseille, France

---

Abstract

A time-domain numerical modeling of transversely isotropic Biot poroelastic waves is proposed. The viscous dissipation occurring in the pores is described using the dynamic permeability model developed by Johnson-Koplik-Dashen (JKD). Some of the coefficients in the Biot-JKD model are proportional to the square root of the frequency. In the time-domain, these coefficients introduce shifted fractional derivatives of order $1/2$, involving a convolution product. Based on a diffusive representation, the convolution kernel is replaced by a finite number of memory variables that satisfy local-in-time ordinary differential equations, resulting in the Biot-DA (diffusive approximation) model. The properties of both the Biot-JKD and the Biot-DA model are analyzed: hyperbolicity, decrease of energy, dispersion. To determine the coefficients of the diffusive approximation, two approaches are analyzed: Gaussian quadratures and optimization methods in the frequency range of interest. The nonlinear optimization is shown to be the better way of determination. A splitting strategy is then applied to approximate numerically the Biot-DA equations. The propagative part is discretized using a fourth-order ADER scheme on a Cartesian grid, whereas the diffusive part is solved exactly. An immersed interface method is implemented to take into account heterogeneous media on a Cartesian grid and to discretize the jump conditions at interfaces. Numerical experiments are presented. Comparisons with analytical solutions show the efficiency and the accuracy of the approach, and some numerical experiments are performed to investigate wave phenomena in complex media, such as multiple scattering across a set of random scatterers.

Keywords: porous media; elastic waves; Biot-JKD model; fractional derivatives; time splitting; finite-difference methods; immersed interface method

---

1. Introduction

A porous medium consists of a solid matrix saturated with a fluid that circulates freely through the pores [1, 2, 3]. Such media are involved e.g. in natural rocks, engineering composites [4] and biological materials [5]. The most widely-used model describing the propagation

---

[*] Corresponding author. Tel.: +33 491 05 46 69.
Email addresses: `emilie.blanc@it.uu.se` (Emilie Blanc), `guillaume.chiavassa@centrale-marseille.fr` (Guillaume Chiavassa), `lombard@lma.cnrs-mrs.fr` (Bruno Lombard)

Preprint submitted to Journal of Computational Physics *February 20, 2014*

of mechanical waves in porous media has been proposed by Biot in 1956 [1, 6]. It includes two classical waves (one ”fast” compressional wave and one shear wave), in addition to a second ”slow” compressional wave, which is highly dependent on the saturating fluid. This slow wave was observed experimentally in 1981 [7], thus confirming the validity of Biot’s theory.

Two frequency regimes have to be distinguished when dealing with poroelastic waves. In the low-frequency range (LF), the flow inside the pores is of Poiseuille type [1]. The viscous efforts are then proportional to the relative velocity of the motion between the fluid and the solid components. In the high-frequency range (HF), modeling the dissipation is a more delicate task. Biot first presented an expression for particular pore geometries [6]. In 1987, Johnson-Koplik-Dashen (JKD) published a general expression for the HF dissipation in the case of random pores [8], where the viscous efforts depend on the square root of the frequency. When writing the evolution equations in the time domain, time fractional derivatives are introduced, which involves convolution products [9].

Since the 90’s, many time-domain simulation methods have been developed in the low-frequency range for isotropic media: see [10] and the introduction of [11] for general reviews. To increase the scope of such numerical methods, two significant difficulties must be tackled. The first one is to take into account more realistic constitutive laws in the simulations. Indeed, rocks or bones for example are anisotropic, and usually described by transversely isotropy. The second difficulty concerns the high-frequency range where many applications are performed, like ultrasonic imaging. Due to the presence of fractional derivatives, the past of the solution needs to be stored, increasing dramatically the memory requirements and the computational time. The aim of this paper is to present a numerical method for the propagation of waves in transversely isotropic media and in the high-frequency range.

In the high-frequency range, only two numerical approaches have been proposed in the literature to integrate the Biot-JKD equations directly in the time-domain. The first approach consists in a straightforward discretization of the fractional derivatives defined by a convolution product in time [12]. In the example given in [12], the solution is stored over 20 time steps. The second approach is based on the diffusive representation of the fractional derivative [13]. The convolution product is replaced by a continuum of memory variables satisfying local differential equations [14]. This continuum is then discretized using Gaussian quadrature formulae [15, 16, 17], resulting in the Biot-DA (diffusive approximation) model. In the example proposed in [13], 25 memory variables are used, which is equivalent, in terms of memory requirement, to storing 25 time steps.

For transversely isotropic poroelastic media, the earliest work in the low-frequency range is based on an operator splitting in conjuction with a Fourier pseudospectral method [18]. Recently, a Cartesian-grid finite volume method has been developed [19]. One of the first work combining anistropic media and high-frequency range is proposed in [20]. However, the diffusive approximation proposed in the latter article has three limitations. Firstly, the quadrature formulae make the convergence towards the original fractional operator very slow. Secondly, in the case of small frequencies, the Biot-DA model does not converge towards the Biot-LF model. Lastly, the number of memory variables required for a given accuracy is not specified.

In our previous works, we focused on isotropic poroelasticity, in the low-frequency range [21, 11, 22], and then in the high-frequency range [23, 24]. Here we extend this approach to transversely isotropic media, introducing also an important improvement concerning the approximation of the fractional derivatives. Thanks to a non linear optimization of the quadrature coefficients, the number of memory variables is drastically reduced. Moreover, the quadrature coefficients are always positive, which ensures the stability of the Biot-DA model and the stability of its numerical discretization.

This article is organized as follows. The original Biot-JKD model is outlined in § 2 and the diffusive representation of fractional derivatives is described. The energy decrease is proven, and a dispersion analysis is done. In § 3, approximation of the diffusive model is presented, leading to the Biot-DA system. The properties of this system are also analyzed: energy, hyperbolicity and dispersion. Determination of the quadrature coefficients involved in the Biot-DA model are investigated in § 3.4. Gaussian quadrature formulae and optimization methods are successively proposed and compared, the latter being finally preferred. The numerical modeling of the Biot-DA system is addressed in § 4, where the equations of evolution are split into two parts: the propagative part is discretized using a fourth-order finite-difference scheme, and the diffusive part is solved exactly. An immersed interface method is implemented to account for the jump conditions and for the geometry of the interfaces on a Cartesian grid when dealing with heterogeneous media. Numerous numerical experiments are presented in § 5, validating the method developed in this paper. In § 6, a conclusion is drawn and some futures lines of research are suggested.

2. Physical modeling

2.1. Biot model

We consider a transversely isotropic porous medium, consisting of a solid matrix saturated with a fluid that circulates freely through the pores [1, 2, 3]. The subscripts 1, 3 represent the x, z axes, where z is the symmetry axis. The perturbations propagate with a wavelength λ.

The Biot model involves 15 positive physical parameters: the density ρ_f, the dynamic viscosity η and the bulk modulus K_f of the fluid, the density ρ_s and the bulk modulus K_s of the grains, the porosity $0 \leqslant \phi \leqslant 1$, the tortuosities $\mathcal{T}_1 \geqslant 1$, $\mathcal{T}_3 \geqslant 1$, the absolute permeabilities at null frequency κ_1, κ_3, and the symmetric definite positive drained elastic matrix $\boldsymbol{C}$

$$\boldsymbol{C} = \begin{pmatrix} c_{11} & c_{13} & 0 & 0 \\ c_{13} & c_{33} & 0 & 0 \\ 0 & 0 & c_{55} & 0 \\ 0 & 0 & 0 & \dfrac{c_{11} - c_{12}}{2} \end{pmatrix}. \tag{1}$$

The linear Biot model is valid if the following hypotheses are satisfied [25]:

- $\mathcal{H}_1$: the wavelength λ is large in comparison with the characteristic radius of the pores r;
- $\mathcal{H}_2$: the amplitudes of the waves in the solid and in the fluid are small;
- $\mathcal{H}_3$: the single fluid phase is continuous;
- $\mathcal{H}_4$: the solid matrix is purely elastic;
- $\mathcal{H}_5$: the thermo-mechanical effects are neglected, which is justified when the saturating fluid is a liquid.

In the validity domain of homogenization theory ($\mathcal{H}_1$), two frequency ranges have to be distinguished. The frontier between the low-frequency (LF) range and the high-frequency (HF) range is reached when the viscous efforts are similar to the inertial effects. The frequency transitions are given by [3]

$$f_{ci} = \frac{\eta\,\phi}{2\,\pi\,\mathcal{T}_i\,\kappa_i\,\rho_f} = \frac{\omega_{ci}}{2\,\pi}, \quad i = 1, 3. \tag{2}$$

Denoting $\boldsymbol{u_s}$ and $\boldsymbol{u_f}$ the solid and fluid displacements, the unknowns in a velocity-stress formulation are the solid velocity $\boldsymbol{v_s} = \frac{\partial \boldsymbol{u_s}}{\partial t}$, the filtration velocity $\boldsymbol{w} = \frac{\partial \boldsymbol{\mathcal{W}}}{\partial t} = \frac{\partial}{\partial t}\phi\,(\boldsymbol{u_f} - \boldsymbol{u_s})$, the elastic symmetric stress tensor $\underline{\boldsymbol{\sigma}}$ and the acoustic pressure p. Under the hypothesis of small perturbations ($\mathcal{H}_2$), the symmetric strain tensor $\underline{\boldsymbol{\varepsilon}}$ is

$$\underline{\boldsymbol{\varepsilon}} = \frac{1}{2}\,(\nabla \boldsymbol{u_s} + \nabla \boldsymbol{u_s}^T). \tag{3}$$

Using the Voigt notation, the stress tensor and the strain tensor are arranged into vectors $\boldsymbol{\sigma}$ and $\boldsymbol{\varepsilon}$

$$\left\{\begin{aligned} &\boldsymbol{\sigma} = (\sigma_{11}\,, \sigma_{33}\,, \sigma_{13})^T, \\ &\boldsymbol{\varepsilon} = (\varepsilon_{11}\,, \varepsilon_{33}\,, 2\,\varepsilon_{13})^T. \end{aligned}\right. \tag{4}$$

Setting

$$\left\{\begin{aligned} &\xi = -\nabla.\boldsymbol{\mathcal{W}}, \quad \boldsymbol{C^u} = \boldsymbol{C} + m\,\boldsymbol{\beta}\,\boldsymbol{\beta}^T, && \text{(5a)} \\ &\boldsymbol{\beta} = (\beta_1\,, \beta_1\,, \beta_3)^T, \quad \beta_1 = 1 - \frac{c_{11} + c_{12} + c_{13}}{3\,K_s}, \quad \beta_3 = 1 - \frac{2\,c_{13} + c_{33}}{3\,K_s}, && \text{(5b)} \\ &K = K_s\,(1 + \phi\,(K_s/K_f - 1)), \quad m = \frac{K_s^2}{K - (2\,c_{11} + c_{33} + 2\,c_{12} + 4\,c_{13})/9}, && \text{(5c)} \end{aligned}\right.$$

where $\boldsymbol{C^u}$ is the undrained elastic matrix and ξ is the rate of fluid, the poroelastic linear constitutive laws are

$$\left\{\begin{aligned} &\boldsymbol{\sigma} = \boldsymbol{C^u}\,\boldsymbol{\varepsilon} - m\,\boldsymbol{\beta}\,\xi, && \text{(6a)} \\ &p = m\,\left(\xi - \boldsymbol{\beta}^T\,\boldsymbol{\varepsilon}\right). && \text{(6b)} \end{aligned}\right.$$

Using (5a) and (5b), we obtain equivalently

$$\left\{\begin{aligned} &\boldsymbol{\sigma} = \boldsymbol{C}\,\boldsymbol{\varepsilon} - \boldsymbol{\beta}\,p, \\ &p = m\,\left(\xi - \boldsymbol{\beta}^T\,\boldsymbol{\varepsilon}\right). \end{aligned}\right. \tag{7}$$

The symmetry of $\underline{\boldsymbol{\sigma}}$ implies compatibility conditions between spatial derivatives of the stresses and the pressure, leading to the Beltrami-Michell equation [26, 27]

$$\begin{aligned} &\frac{\partial^2 \sigma_{13}}{\partial x\,\partial z} = \Theta_0\,\frac{\partial^2 \sigma_{11}}{\partial x^2} + \Theta_1\,\frac{\partial^2 \sigma_{33}}{\partial x^2} + \Theta_2\,\frac{\partial^2 p}{\partial x^2} + \Theta_3\,\frac{\partial^2 \sigma_{11}}{\partial z^2} + \Theta_0\,\frac{\partial^2 \sigma_{33}}{\partial z^2} + \Theta_4\,\frac{\partial^2 p}{\partial z^2}, \\ &\Theta_0 = -c_{55}\,\frac{c_{13}}{c_{11}\,c_{33} - c_{13}^2}, \quad \Theta_1 = -\frac{c_{11}}{c_{13}}\,\Theta_0, \quad \Theta_2 = \beta_1\,\Theta_0 + \beta_3\,\Theta_1, \\ &\Theta_3 = -\frac{c_{33}}{c_{13}}\,\Theta_0, \quad \Theta_4 = \beta_3\,\Theta_0 + \beta_1\,\Theta_3. \end{aligned} \tag{8}$$

If the medium is isotropic and in the elastic limit case ($\beta_1 = \beta_3 = 0$), we recover the usual equation of Barré de Saint-Venant.

Introducing the densities

$$\rho = \phi\,\rho_f + (1-\phi)\,\rho_s, \quad \rho_{wi} = \frac{\mathcal{T}_i}{\phi}\,\rho_f, \quad i = 1, 3, \tag{9}$$

the conservation of momentum yields

$$\left\{ \begin{aligned} &\rho\,\frac{\partial \boldsymbol{v_s}}{\partial t} + \rho_f\,\frac{\partial \boldsymbol{w}}{\partial t} = \nabla\,.\,\underline{\boldsymbol{\sigma}}, &\text{(10a)}\\ &\rho_f\,\frac{\partial \boldsymbol{v_s}}{\partial t} + \operatorname{diag}(\rho_{wi})\,\frac{\partial \boldsymbol{w}}{\partial t} + \operatorname{diag}\left(\frac{\eta}{\kappa_i}\,F_i(t)\right) * \boldsymbol{w} = -\nabla\,p, &\text{(10b)} \end{aligned} \right.$$

where $\operatorname{diag}(d_i)$ denotes the 2×2 diagonal matrix $\left(\begin{smallmatrix} d_1 & 0 \\ 0 & d_3 \end{smallmatrix}\right)$, $*$ denotes the time convolution product and $F_i(t)$ are viscous operators. In LF, the flow in the pores is of Poiseuille type, and the dissipation efforts in (10b) are given by

$$F_i(t) \equiv F_i^{LF}(t) = \delta(t) \Longleftrightarrow F_i^{LF}(t) * w_i(x,z,t) = w_i(x,z,t), \quad i = 1, 3, \tag{11}$$

where δ is the Dirac distribution, which amounts to the Darcy's law.

2.2. High frequency dissipation: the JKD model

In HF, a Prandtl boundary layer occurs at the surface of the pores, where the effects of viscosity are significant. Its width is inversely proportional to the square root of the frequency. Biot first presented in 1956 an expression of the dissipation process for particular pore geometries [6]. In 1987, a general expression of the viscous operator has been proposed by Johnson, Koplik and Dashen, valid for random networks of pores with constant radii [8]. This function is the most-simple one fitting the LF and HF limits and leading to a causal model. The only additional parameters are the viscous characteristic length Λ_i. We take

$$P_i = \frac{4\,\mathcal{T}_i\,\kappa_i}{\phi\,\Lambda_i^2}, \quad \Omega_i = \frac{\omega_{ci}}{P_i} = \frac{\eta\,\phi^2\,\Lambda_i^2}{4\,\mathcal{T}_i^2\,\kappa_i^2\,\rho_f}, \quad i = 1, 3, \tag{12}$$

where P_i are the Pride number (typically $P_i \approx 1/2$). Based on the Fourier transform in time, $\widehat{F}_i(\omega) = \mathcal{F}\,(F_i(t)) = \int_{\mathbb{R}} F_i(t) e^{-j\omega t}\,dt$, the viscous operators given by the JKD model are

$$\begin{aligned} \widehat{F}_i^{JKD}(\omega) &= \left(1 + j\,\omega\,\frac{4\,\mathcal{T}_i^2\,\kappa_i^2\,\rho_f}{\eta\,\Lambda_i^2\,\phi^2}\right)^{1/2}, \\ &= \left(1 + j\,P_i\,\frac{\omega}{\omega_{ci}}\right)^{1/2}, \\ &= \frac{1}{\sqrt{\Omega_i}}\,(\Omega_i + j\,\omega)^{1/2}. \end{aligned} \tag{13}$$

Therefore, the terms $F_i(t) * w_i(x,z,t)$ involved in (6b) are

$$\begin{aligned} F_i^{JKD}(t) * w_i(x,z,t) &= \mathcal{F}^{-1}\left(\frac{1}{\sqrt{\Omega_i}}\,(\Omega_i + j\,\omega)^{1/2}\widehat{w}_i(x,z,\omega)\right), \\ &= \frac{1}{\sqrt{\Omega_i}}\,(D + \Omega_i)^{1/2} w_i(x,z,t). \end{aligned} \tag{14}$$

In the last relation of (14), $(D+\Omega_i)^{1/2}$ is an operator. $D^{1/2}$ is a fractional derivative in time of order $1/2$, generalizing the usual derivative characterized by $\frac{\partial w_i}{\partial t} = \mathcal{F}^{-1}\left(j\,\omega\,\widehat{w_i}\right)$. The notation $(D+\Omega_i)^{1/2}$ accounts for the shift Ω_i in (14).

2.3. The Biot-JKD equations of evolution

The system (10) is rearranged by separating $\frac{\partial \boldsymbol{v_s}}{\partial t}$ and $\frac{\partial \boldsymbol{w}}{\partial t}$ and using the definitions of $\boldsymbol{\varepsilon}$ and ξ. Taking

$$\gamma_i = \frac{\eta}{\kappa_i}\,\frac{\rho}{\chi_i}\,\frac{1}{\sqrt{\Omega_i}}, \quad i = 1, 3, \tag{15}$$

one obtains the following system of evolution equations

$$\left\{\begin{array}{lr}
\dfrac{\partial v_{s1}}{\partial t} - \dfrac{\rho_{w1}}{\chi_1}\left(\dfrac{\partial \sigma_{11}}{\partial x} + \dfrac{\partial \sigma_{13}}{\partial z}\right) - \dfrac{\rho_f}{\chi_1}\,\dfrac{\partial p}{\partial x} = \dfrac{\rho_f}{\rho}\,\gamma_1\,(D+\Omega_1)^{1/2}\,w_1 + G_{v_{s1}}, & \text{(16a)}\\[2ex]
\dfrac{\partial v_{s3}}{\partial t} - \dfrac{\rho_{w3}}{\chi_3}\left(\dfrac{\partial \sigma_{13}}{\partial x} + \dfrac{\partial \sigma_{33}}{\partial z}\right) - \dfrac{\rho_f}{\chi_3}\,\dfrac{\partial p}{\partial z} = \dfrac{\rho_f}{\rho}\,\gamma_3\,(D+\Omega_3)^{1/2}\,w_3 + G_{v_{s3}}, & \text{(16b)}\\[2ex]
\dfrac{\partial w_1}{\partial t} + \dfrac{\rho_f}{\chi_1}\left(\dfrac{\partial \sigma_{11}}{\partial x} + \dfrac{\partial \sigma_{13}}{\partial z}\right) + \dfrac{\rho}{\chi_1}\,\dfrac{\partial p}{\partial x} = -\gamma_1\,(D+\Omega_1)^{1/2}\,w_1 + G_{w_1}, & \text{(16c)}\\[2ex]
\dfrac{\partial w_3}{\partial t} + \dfrac{\rho_f}{\chi_3}\left(\dfrac{\partial \sigma_{13}}{\partial x} + \dfrac{\partial \sigma_{33}}{\partial z}\right) + \dfrac{\rho}{\chi_3}\,\dfrac{\partial p}{\partial z} = -\gamma_3\,(D+\Omega_3)^{1/2}\,w_3 + G_{w_3}, & \text{(16d)}\\[2ex]
\dfrac{\partial \sigma_{11}}{\partial t} - c_{11}^u\,\dfrac{\partial v_{s1}}{\partial x} - c_{13}^u\,\dfrac{\partial v_{s3}}{\partial z} - m\beta_1\left(\dfrac{\partial w_1}{\partial x} + \dfrac{\partial w_3}{\partial z}\right) = G_{\sigma_{11}}, & \text{(16e)}\\[2ex]
\dfrac{\partial \sigma_{13}}{\partial t} - c_{55}^u\left(\dfrac{\partial v_{s3}}{\partial x} + \dfrac{\partial v_{s1}}{\partial z}\right) = G_{\sigma_{13}}, & \text{(16f)}\\[2ex]
\dfrac{\partial \sigma_{33}}{\partial t} - c_{13}^u\,\dfrac{\partial v_{s1}}{\partial x} - c_{33}^u\,\dfrac{\partial v_{s3}}{\partial z} - m\beta_3\left(\dfrac{\partial w_1}{\partial x} + \dfrac{\partial w_3}{\partial z}\right) = G_{\sigma_{33}}, & \text{(16g)}\\[2ex]
\dfrac{\partial p}{\partial t} + m\left(\beta_1\,\dfrac{\partial v_{s1}}{\partial x} + \beta_3\,\dfrac{\partial v_{s3}}{\partial z} + \dfrac{\partial w_1}{\partial x} + \dfrac{\partial w_3}{\partial z}\right) = G_p. & \text{(16h)}
\end{array}\right.$$

The terms $G_{v_{s1}}$, $G_{v_{s3}}$, G_{w_1}, G_{w_3}, $G_{\sigma_{11}}$, $G_{\sigma_{13}}$, $G_{\sigma_{33}}$ and G_p have been introduced to model the forcing.

2.4. The diffusive representation

The shifted fractional derivatives [28] in (14) can be written ($i = 1, 3$)

$$(D+\Omega_i)^{1/2} w_i(x,z,t) = \int_0^t \frac{e^{-\Omega_i(t-\tau)}}{\sqrt{\pi\,(t-\tau)}}\left(\frac{\partial w_i}{\partial t}(x,z,\tau) + \Omega_i\,w_i(x,z,\tau)\right)d\tau. \tag{17}$$

The operators $(D+\Omega_i)^{1/2}$ are not local in time and involve the entire time history of $\boldsymbol{w}$. Based on Euler's Gamma function, the diffusive representation of the totally monotone function $\frac{1}{\sqrt{\pi\,t}}$ is [14]

$$\frac{1}{\sqrt{\pi\,t}} = \frac{1}{\pi}\int_0^\infty \frac{1}{\sqrt{\theta}}\,e^{-\theta t}d\theta. \tag{18}$$

Substituting (18) into (17) gives

$$(D+\Omega_i)^{1/2} w_i(x,z,t) = \frac{1}{\pi}\int_0^{\infty} \frac{1}{\sqrt{\theta}}\, \psi_i(x,z,\theta,t)\, d\theta, \tag{19}$$

where the memory variables are defined as

$$\psi_i(x,z,\theta,t) = \int_0^t e^{-(\theta+\Omega_i)(t-\tau)} \left(\frac{\partial w_i}{\partial t}(x,z,\tau) + \Omega_i\, w_i(x,z,\tau)\right) d\tau. \tag{20}$$

For the sake of clarity, the dependence on Ω_i and w_i are omitted in ψ_i. From (20), it follows that the two memory variables ψ_i satisfy the ordinary differential equation

$$\left\{\begin{array}{ll} \dfrac{\partial \psi_i}{\partial t} = -(\theta+\Omega_i)\,\psi_i + \dfrac{\partial w_i}{\partial t} + \Omega_i\, w_i, & \text{(21a)}\\[2ex] \psi_i(x,z,\theta,0) = 0. & \text{(21b)} \end{array}\right.$$

The diffusive representation therefore transforms a non-local problem (17) into a continuum of local problems (19). It should be emphasized at this point that no approximation have been made up to now. The computational advantages of the diffusive representation will be seen in § 3 and 5, where the discretization of (19) and (21a) will yield a numerically tractable formulation.

2.5. Energy of Biot-JKD

Now, we express the energy of the Biot-JKD model (16).

Proposition 1 (Decrease of the energy). *Let us consider the Biot-JKD model (16) without forcing, and let us denote*

$$E = E_1 + E_2 + E_3, \tag{22}$$

with

$$\begin{aligned} E_1 &= \frac{1}{2}\int_{\mathbb{R}^2} \left(\rho\, \boldsymbol{v_s}^T \boldsymbol{v_s} + 2\,\rho_f\, \boldsymbol{v_s}^T \boldsymbol{w} + \boldsymbol{w}^T \operatorname{diag}(\rho_{wi})\, \boldsymbol{w}\right) dx\, dz,\\ E_2 &= \frac{1}{2}\int_{\mathbb{R}^2} \left((\boldsymbol{\sigma} + p\,\boldsymbol{\beta})^T\, \boldsymbol{C}^{-1}\, (\boldsymbol{\sigma} + p\,\boldsymbol{\beta}) + \frac{1}{m}\, p^2\right) dx\, dz,\\ E_3 &= \frac{1}{2}\int_{\mathbb{R}^2} \frac{\eta}{\pi}\int_0^{\infty} (\boldsymbol{w}-\boldsymbol{\psi})^T \operatorname{diag}\left(\frac{1}{\kappa_i\,\sqrt{\Omega_i\,\theta}\,(\theta+2\,\Omega_i)}\right) (\boldsymbol{w}-\boldsymbol{\psi})\, d\theta\, dx\, dz. \end{aligned} \tag{23}$$

Then, E is an energy which satisfies

$$\begin{aligned} \frac{dE}{dt} = -\int_{\mathbb{R}^2} \frac{\eta}{\pi}\int_0^{\infty} &\left\{\boldsymbol{\psi}^T \operatorname{diag}\left(\frac{\theta+\Omega_i}{\kappa_i\,\sqrt{\Omega_i\,\theta}\,(\theta+2\,\Omega_i)}\right) \boldsymbol{\psi}\right.\\ &\left. +\boldsymbol{w}^T \operatorname{diag}\left(\frac{\Omega_i}{\kappa_i\,\sqrt{\Omega_i\,\theta}\,(\theta+2\,\Omega_i)}\right) \boldsymbol{w}\right\} d\theta\, dx\, dz \;\leqslant\; 0. \end{aligned} \tag{24}$$

Proposition 1 is proven in Appendix A. It calls for the following comments:

- the Biot-JKD model is stable;

- when the viscosity of the saturating fluid is neglected ($\eta = 0$), the energy of the system is conserved;
- the terms E_1 and E_2 in (23) have a clear physical significance: E_1 is the kinetic energy, and E_2 is the strain energy;
- the energy analysis is valid for continuously variable parameters.

2.6. Dispersion analysis

In this section, we derive the dispersion relation of the waves which propagate in a poroelastic medium. This relation describes the frequency dependence of phase velocities and attenuations of waves. For this purpose, we search for a general plane wave solution of (16)

$$\left\{ \begin{aligned} &\boldsymbol{V} = (v_1\,,\, v_3\,,\, w_1\,,\, w_3)^T = \boldsymbol{V_0}\, e^{j(\omega t - \boldsymbol{k}.\boldsymbol{r})}, \\ &\boldsymbol{T} = (\sigma_{11}\,,\, \sigma_{13}\,,\, \sigma_{33}\,,\, -p)^T = \boldsymbol{T_0}\, e^{j(\omega t - \boldsymbol{k}.\boldsymbol{r})}, \end{aligned} \right. \tag{25}$$

where $\boldsymbol{k} = k\,(\cos(\varphi),\ \sin(\varphi))^T$ is the wavevector, k is the wavenumber, $\boldsymbol{V_0}$ and $\boldsymbol{T_0}$ are the polarizations, $\boldsymbol{r} = (x,\ z)^T$ is the position, $\omega = 2\,\pi\,f$ is the angular frequency and f is the frequency. On one hand, (25) is injected in (16e)-(16h). We obtain the 4×4 linear system:

$$\omega\, \boldsymbol{T} = -k\, \underbrace{\begin{pmatrix} c_{11}^u\, c_\varphi & c_{13}^u\, s_\varphi & \beta_1\, m\, c_\varphi & \beta_1\, m\, s_\varphi \\ c_{55}^u\, s_\varphi & c_{55}^u\, c_\varphi & 0 & 0 \\ c_{13}^u\, c_\varphi & c_{33}^u\, s_\varphi & \beta_3\, m\, c_\varphi & \beta_3\, m\, s_\varphi \\ \beta_1\, m\, c_\varphi & \beta_3\, m\, s_\varphi & m\, c_\varphi & m\, s_\varphi \end{pmatrix}}_{\boldsymbol{C}}\, \boldsymbol{V}, \tag{26}$$

where $c_\varphi = \cos(\varphi)$ and $s_\varphi = \sin(\varphi)$. On the other hand, substituting (25) into (16a)-(16d) gives another 4×4 linear system:

$$-k\, \underbrace{\begin{pmatrix} c_\varphi & s_\varphi & 0 & 0 \\ 0 & c_\varphi & s_\varphi & 0 \\ 0 & 0 & 0 & c_\varphi \\ 0 & 0 & 0 & s_\varphi \end{pmatrix}}_{\boldsymbol{\mathcal{L}}}\, \boldsymbol{T} = \omega\, \underbrace{\begin{pmatrix} \rho & 0 & \rho_f & 0 \\ 0 & \rho & 0 & \rho_f \\ \rho_f & 0 & \dfrac{\widehat{Y}_1^{JKD}(\omega)}{j\,\omega} & 0 \\ 0 & \rho_f & 0 & \dfrac{\widehat{Y}_3^{JKD}(\omega)}{j\,\omega} \end{pmatrix}}_{\boldsymbol{\Gamma}}\, \boldsymbol{V}, \tag{27}$$

where $\widehat{Y}_1^{JKD}$ and $\widehat{Y}_3^{JKD}$ are the viscodynamic operators [29]:

$$\widehat{Y}_i^{JKD} = j\,\omega\,\rho_{wi} + \frac{\eta}{\kappa_i}\,\widehat{F}_i^{JKD}(\omega), \quad i = 1, 3. \tag{28}$$

Since the matrix $\boldsymbol{\Gamma}$ is invertible, the equations (26) and (27) lead to the eigenproblem

$$\boldsymbol{\Gamma}^{-1}\, \boldsymbol{\mathcal{L}}\, \boldsymbol{C}\, \boldsymbol{V} = \left(\frac{\omega}{k}\right)^2 \boldsymbol{V}. \tag{29}$$

The equation (29) is solved numerically. The two quasi-compressional waves are denoted qP_f (fast) and qP_s (slow), and the quasi-shear wave is denoted qS. The wavenumbers thus obtained depend on the frequency and on the angle φ. One of the eigenvalues is zero with multiplicity two, and the other non-zero eigenvalues correspond to the wave modes $\pm k_{pf}(\omega, \varphi)$, $\pm k_{ps}(\omega, \varphi)$ and $\pm k_s(\omega, \varphi)$. Therefore three waves propagates symmetrically along the directions $\cos(\varphi)\,x + \sin(\varphi)\,z$ and $-\cos(\varphi)\,x - \sin(\varphi)\,z$.

The wavenumbers give the phase velocities $c_{pf}(\omega, \varphi) = \omega / \Re\mathrm{e}(k_{pf})$, $c_{ps}(\omega, \varphi) = \omega / \Re\mathrm{e}(k_{ps})$, and $c_s(\omega, \varphi) = \omega / \Re\mathrm{e}(k_s)$, with $0 < c_{ps} < c_{pf}$ and $0 < c_s$. The attenuations $\alpha_{pf}(\omega, \varphi) = -\Im\mathrm{m}(k_{pf})$, $\alpha_{ps}(\omega, \varphi) = -\Im\mathrm{m}(k_{ps})$ and $\alpha_s(\omega, \varphi) = -\Im\mathrm{m}(k_s)$ are also deduced. Both the phase velocities and the attenuations of Biot-LF and Biot-JKD are strictly increasing functions of the frequency. The high-frequency limits ($\omega \to \infty$ in (29)) of phase velocities $c_{pf}^{\infty}(\varphi)$, $c_{ps}^{\infty}(\varphi)$ and $c_s^{\infty}(\varphi)$ are recovered by diagonalizing the left-hand side of (16).

In figure 1, the physical parameters are those of medium Ω_0 (cf table 1), where the frequencies of transition are $f_{c1} = 25.5$ kHz, $f_{c3} = 85$ kHz. Figure 1 shows the dispersion curves in terms of the frequency at $\varphi = 0$ rad. Note that the vertical scales of the figures are radically different for the three waves. The high-frequency limit of the phase velocities of the quasi-compressional waves are $c_{pf}^{\infty}(0) = 5244$ m/s and $c_{ps}^{\infty}(0) = 975$ m/s, which justifies the denomination "fast" and "slow". Figure 1 calls for the following comments:

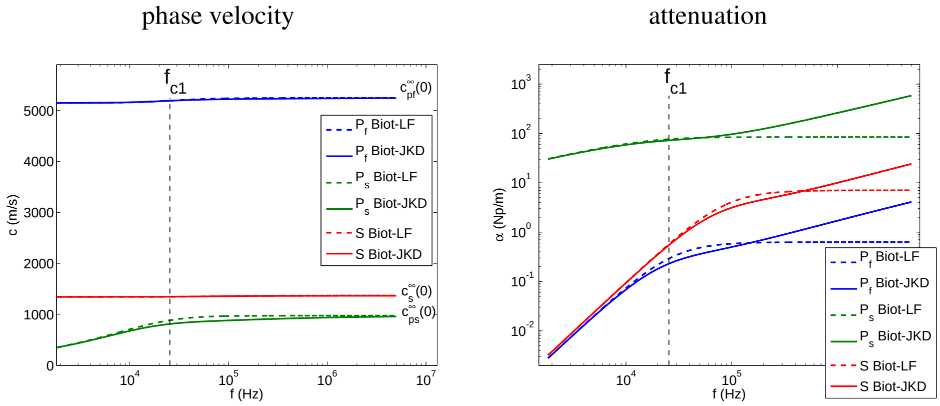

Figure 1: dispersion curves in terms of the frequency. Comparison between Biot-LF and Biot-JKD models at $\varphi = 0$ rad.

- when $f < f_{ci}$, the Biot-JKD and Biot-LF dispersion curves are very similar as might be expected, since $\widehat{F}_i^{JKD}(0) = \widehat{F}_i^{LF}(0) = 1$;

- the frequency evolution of the phase velocity and of the attenuation is radically different for the three waves, whatever the chosen model (LF or JKD): the effect of viscous losses is negligible on the fast wave, small on the shear wave, whereas it is very important on the slow wave;

- when $f \ll f_{ci}$, the slow compressional wave is almost static [30, 27]. When $f > f_{ci}$, the slow wave propagates but is greatly attenuated.

Taking

$$\boldsymbol{U}_1 = \begin{pmatrix} 1 & 0 & 0 & 0 \\ 0 & 0 & 1 & 0 \\ 0 & 0 & 0 & 1 \\ 0 & 0 & 0 & 0 \end{pmatrix}, \quad \boldsymbol{U}_3 = \begin{pmatrix} 0 & 0 & 1 & 0 \\ 0 & 1 & 0 & 0 \\ 0 & 0 & 0 & 0 \\ 0 & 0 & 0 & 1 \end{pmatrix}, \tag{30}$$

the energy velocity vector $\boldsymbol{V}_e$ is [18, 31]:

$$\left\{ \begin{array}{l} \boldsymbol{V}_e = \dfrac{\langle \boldsymbol{P} \rangle}{\langle E_s + E_k \rangle} = \dfrac{\langle \boldsymbol{P} \rangle}{\langle E \rangle}, \\ \langle \boldsymbol{P} \rangle = -\dfrac{1}{2}\, \Re\mathrm{e}\left(\left(\overrightarrow{e_x}\, (\boldsymbol{U}_1.\boldsymbol{T})^T + \overrightarrow{e_z}\, (\boldsymbol{U}_3.\boldsymbol{T})^T \right) . \overline{\boldsymbol{V}} \right), \\ \langle E \rangle = \dfrac{1}{4}\, \Re\mathrm{e}\left(\left(1 + \dfrac{(\omega/k)^2}{|\omega/k|^2} \right) \boldsymbol{V}^T\, \boldsymbol{\Gamma}\, \overline{\boldsymbol{V}} \right), \end{array} \right. \tag{31}$$

where $\overline{\boldsymbol{V}}$ is the complex conjugate of $\boldsymbol{V}$, $\langle \boldsymbol{P} \rangle$ is the Umov-Poynting vector, $\langle E_k \rangle$ and $\langle E_s \rangle$ are the average kinetic and strain energy densities, and $\langle E \rangle$ is the mean energy density. The theoretical wavefronts are the locus of the end of energy velocity vector $\boldsymbol{V}_e$ multiplied by the time of propagation. We will use this property in § 5 to validate the simulations.

3. The Biot-DA (diffusive approximation) model

The aim of this section is to approximate the Biot-JKD model, using a numerically tractable approach.

3.1. Diffusive approximation

The diffusive representation of fractional derivatives (19) is approximated by using a quadrature formula on N points, with weights a_ℓ^i and abcissae θ_ℓ^i $(i = 1, 3)$:

$$\begin{aligned} (D + \Omega_i)^{1/2} w_i(x, z, t) &= \frac{1}{\pi} \int_0^\infty \frac{1}{\sqrt{\theta}} \psi^i(x, z, \theta, t)\, d\theta \\ &\simeq \sum_{\ell=1}^{N} a_\ell^i\, \psi^i(x, z, \theta_\ell^i, t), \\ &\equiv \sum_{\ell=1}^{N} a_\ell^i\, \psi_\ell^i(x, z, t). \end{aligned} \tag{32}$$

From (21a), the $2\,N$ memory variables ψ_ℓ^i satisfy the ordinary differential equations

$$\left\{ \begin{array}{l} \dfrac{\partial\, \psi_\ell^i}{\partial\, t} = -(\theta_\ell^i + \Omega_i)\, \psi_\ell^i + \dfrac{\partial\, w_i}{\partial\, t} + \Omega_i\, w_i, \\ \psi_\ell^i(x, z, 0) = 0. \end{array} \right. \tag{33}$$

3.2. The Biot-DA first-order system

The fractional derivatives involved in the Biot-JKD system (16) are replaced by their diffusive approximation (32), with evolution equations (33). After some algebraic operations, the Biot-DA system is written as a first-order system in time and in space, used in the numerical simulations of § 5 ($j = 1, \cdots N$)

$$\begin{cases}
\dfrac{\partial v_{s1}}{\partial t} - \dfrac{\rho_{w1}}{\chi_1}\left(\dfrac{\partial \sigma_{11}}{\partial x} + \dfrac{\partial \sigma_{13}}{\partial z}\right) - \dfrac{\rho_f}{\chi_1}\dfrac{\partial p}{\partial x} = \dfrac{\rho_f}{\rho}\gamma_1 \displaystyle\sum_{\ell=1}^{N} a_\ell^1 \psi_\ell^1 + G_{v_{s1}}, \\
\dfrac{\partial v_{s3}}{\partial t} - \dfrac{\rho_{w3}}{\chi_3}\left(\dfrac{\partial \sigma_{13}}{\partial x} + \dfrac{\partial \sigma_{33}}{\partial z}\right) - \dfrac{\rho_f}{\chi_3}\dfrac{\partial p}{\partial z} = \dfrac{\rho_f}{\rho}\gamma_3 \displaystyle\sum_{\ell=1}^{N} a_\ell^3 \psi_\ell^3 + G_{v_{s3}}, \\
\dfrac{\partial w_1}{\partial t} + \dfrac{\rho_f}{\chi_1}\left(\dfrac{\partial \sigma_{11}}{\partial x} + \dfrac{\partial \sigma_{13}}{\partial z}\right) + \dfrac{\rho}{\chi_1}\dfrac{\partial p}{\partial x} = -\gamma_1 \displaystyle\sum_{\ell=1}^{N} a_\ell^1 \psi_\ell^1 + G_{w_1}, \\
\dfrac{\partial w_3}{\partial t} + \dfrac{\rho_f}{\chi_3}\left(\dfrac{\partial \sigma_{13}}{\partial x} + \dfrac{\partial \sigma_{33}}{\partial z}\right) + \dfrac{\rho}{\chi_3}\dfrac{\partial p}{\partial z} = -\gamma_3 \displaystyle\sum_{\ell=1}^{N} a_\ell^3 \psi_\ell^3 + G_{w_3}, \\
\dfrac{\partial \sigma_{11}}{\partial t} - c_{11}^u \dfrac{\partial v_{s1}}{\partial x} - c_{13}^u \dfrac{\partial v_{s3}}{\partial z} - m\beta_1 \left(\dfrac{\partial w_1}{\partial x} + \dfrac{\partial w_3}{\partial z}\right) = G_{\sigma_{11}}, \\
\dfrac{\partial \sigma_{13}}{\partial t} - c_{55}^u \left(\dfrac{\partial v_{s3}}{\partial x} + \dfrac{\partial v_{s1}}{\partial z}\right) = G_{\sigma_{13}}, \\
\dfrac{\partial \sigma_{33}}{\partial t} - c_{13}^u \dfrac{\partial v_{s1}}{\partial x} - c_{33}^u \dfrac{\partial v_{s3}}{\partial z} - m\beta_3 \left(\dfrac{\partial w_1}{\partial x} + \dfrac{\partial w_3}{\partial z}\right) = G_{\sigma_{33}}, \\
\dfrac{\partial p}{\partial t} + m\left(\beta_1 \dfrac{\partial v_{s1}}{\partial x} + \beta_3 \dfrac{\partial v_{s3}}{\partial z} + \dfrac{\partial w_1}{\partial x} + \dfrac{\partial w_3}{\partial z}\right) = G_p, \\
\dfrac{\partial \psi_j^1}{\partial t} + \dfrac{\rho_f}{\chi_1}\left(\dfrac{\partial \sigma_{11}}{\partial x} + \dfrac{\partial \sigma_{13}}{\partial z}\right) + \dfrac{\rho}{\chi_1}\dfrac{\partial p}{\partial x} = \Omega_1 w_1 - \gamma_1 \displaystyle\sum_{\ell=1}^{N} a_\ell^1 \psi_\ell^1 - (\theta_j^1 + \Omega_1)\psi_j^1 + G_{w_1}, \\
\dfrac{\partial \psi_j^3}{\partial t} + \dfrac{\rho_f}{\chi_3}\left(\dfrac{\partial \sigma_{13}}{\partial x} + \dfrac{\partial \sigma_{33}}{\partial z}\right) + \dfrac{\rho}{\chi_3}\dfrac{\partial p}{\partial z} = \Omega_3 w_3 - \gamma_3 \displaystyle\sum_{\ell=1}^{N} a_\ell^3 \psi_\ell^3 - (\theta_j^3 + \Omega_3)\psi_j^3 + G_{w_3}.
\end{cases} \tag{34}$$

Taking the vector of unknowns

$$\boldsymbol{U} = (v_{s1}\,,\, v_{s3}\,,\, w_1\,,\, w_3\,,\, \sigma_{11}\,,\, \sigma_{13}\,,\, \sigma_{33}\,,\, p\,,\, \psi_1^1\,,\, \psi_1^3\,,\, \cdots\,,\, \psi_N^1\,,\, \psi_N^3)^T, \tag{35}$$

and the forcing

$$\boldsymbol{G} = \left(G_{v_{s1}}\,,\, G_{v_{s3}}\,,\, G_{w_1}\,,\, G_{w_3}\,,\, G_{\sigma_{11}}\,,\, G_{\sigma_{13}}\,,\, G_{\sigma_{33}}\,,\, G_p\,,\, G_{w_1}\,,\, G_{w_3}\,,\, G_{w_1}\,,\, G_{w_3}\right)^T, \tag{36}$$

the system (34) is written in the form:

$$\frac{\partial \boldsymbol{U}}{\partial t} + \boldsymbol{A}\,\frac{\partial \boldsymbol{U}}{\partial x} + \boldsymbol{B}\,\frac{\partial \boldsymbol{U}}{\partial z} = -\boldsymbol{S}\,\boldsymbol{U} + \boldsymbol{G}, \tag{37}$$

where $\boldsymbol{A}$ and $\boldsymbol{B}$ are the $(2\,N + 8) \times (2\,N + 8)$ propagation matrices and $\boldsymbol{S}$ is the diffusive matrix (given in Appendix B). The number of unknowns increases linearly with the number of memory variables. Only the matrix $\boldsymbol{S}$ depends on the coefficients of the diffusive approximation.

3.3. Properties

Some properties are stated to characterize the first-order differential system (34). First, one notes that the only difference between the Biot-LF model, the Biot-JKD model and the Biot-DA model occurs in the viscous operators

$$\widehat{F}_i(\omega) = \begin{cases} \widehat{F}_i^{LF}(\omega) = 1 & \text{Biot-LF}, \\ \widehat{F}_i^{JKD}(\omega) = \dfrac{1}{\sqrt{\Omega_i}}\,(\Omega_i + j\,\omega)^{1/2} & \text{Biot-JKD}, \\ \widehat{F}_i^{DA}(\omega) = \dfrac{\Omega_i + j\,\omega}{\sqrt{\Omega_i}} \displaystyle\sum_{\ell=1}^{N} \dfrac{a_\ell^i}{\theta_\ell^i + \Omega_i + j\,\omega} & \text{Biot-DA}. \end{cases} \tag{38}$$

The dispersion analysis of the Biot-DA model is obtained by replacing the viscous operators $\widehat{F}_i^{JKD}(\omega)$ by $\widehat{F}_i^{DA}(\omega)$ in (28). One of the eigenvalues of $\boldsymbol{\Gamma}^{-1}\,\boldsymbol{\mathcal{L}}\,\boldsymbol{C}$ (29) is still zero with multiplicity two, and the other non-zero eigenvalues correspond to the wave modes $\pm k_{pf}(\omega,\varphi)$, $\pm k_{ps}(\omega,\varphi)$ and $\pm k_s(\omega,\varphi)$. Consequently, the diffusive approximation does not introduce spurious wave.

Proposition 2. *The eigenvalues of the matrix* $\boldsymbol{M} = \cos(\varphi)\,\boldsymbol{A} + \sin(\varphi)\,\boldsymbol{B}$ *are*

$$sp(\boldsymbol{M}) = \left\{0\,,\ \pm c_{pf}^{\infty}(\varphi)\,,\ \pm c_{ps}^{\infty}(\varphi)\,,\ \pm c_{s}^{\infty}(\varphi)\right\}, \tag{39}$$

with 0 *being of multiplicity* $2\,N + 2$.

The non-zero eigenvalues do not depend on the viscous operators $\widehat{F}_i(\omega)$. Consequently, the high-frequency limits of the phase velocities $c_{pf}^{\infty}(\varphi)$, $c_{ps}^{\infty}(\varphi)$ and $c_{s}^{\infty}(\varphi)$, defined in § 2.6, are the same for both Biot-LF, Biot-JKD and Biot-DA models. An argumentation similar to [19] shows that the matrix $\boldsymbol{M}$ is diagonalizable for all φ in $[0, 2\,\pi[$, with real eigenvalues. The three models are therefore hyperbolic.

Proposition 3 (Decrease of the energy). *An energy analysis of (34) is performed. Let us consider the Biot-DA model (34) without forcing, and let us denote*

$$E = E_1 + E_2 + E_3, \tag{40}$$

where

$$\begin{aligned} E_1 &= \frac{1}{2}\int_{\mathbb{R}^2}\left(\rho\,\boldsymbol{v_s}^T\,\boldsymbol{v_s} + 2\,\rho_f\,\boldsymbol{v_s}^T\,\boldsymbol{w} + \boldsymbol{w}^T\,\mathrm{diag}\,(\rho_{wi})\,\boldsymbol{w}\right)dx\,dz, \\ E_2 &= \frac{1}{2}\int_{\mathbb{R}^2}\left((\boldsymbol{\sigma} + p\,\boldsymbol{\beta})^T\,\boldsymbol{C}^{-1}\,(\boldsymbol{\sigma} + p\,\boldsymbol{\beta}) + \frac{1}{m}\,p^2\right)dx\,dz, \\ E_3 &= \frac{1}{2}\int_{\mathbb{R}^2}\frac{\eta}{\pi}\sum_{\ell=1}^{N}(\boldsymbol{w} - \boldsymbol{\psi_\ell})^T\,\mathrm{diag}\left(\frac{a_\ell^i}{\kappa_i\,\sqrt{\Omega_i\,\theta_\ell^i\,(\theta_\ell^i + 2\,\Omega_i)}}\right)(\boldsymbol{w} - \boldsymbol{\psi_\ell})\,dx\,dz. \end{aligned} \tag{41}$$

Then, E satisfies

$$\begin{aligned} \frac{dE}{dt} = -\int_{\mathbb{R}^2} \frac{\eta}{\pi} \sum_{\ell=1}^{N} \Bigg\{ & \boldsymbol{\psi_\ell}^T \operatorname{diag}\left(\frac{a_\ell^i\,(\theta_\ell^i + \Omega_i)}{\kappa_i\,\sqrt{\Omega_i\,\theta_\ell^i\,(\theta_\ell^i + 2\,\Omega_i)}} \right) \boldsymbol{\psi_\ell} \\ & + \boldsymbol{w}^T \operatorname{diag}\left(\frac{a_\ell^i\,\Omega_i}{\kappa_i\,\sqrt{\Omega_i\,\theta_\ell^i\,(\theta_\ell^i + 2\,\Omega_i)}} \right) \boldsymbol{w} \Bigg\}\, dx\,dz. \end{aligned} \tag{42}$$

The proof of the proposition 3 is similar to the proof of the proposition 1 and will not be repeated here. Proposition 3 calls the following comments:

- the terms E_1 and E_2 are the same in both the Biot-DA and Biot-JKD models;
- E_3 and the time evolution of E are modified by the diffusive approximation;
- the abscissae θ_ℓ^i are always positive, as explained in § 3.4, but not necessarily the weights a_ℓ^i. Consequently, in the general case, we cannot say that the Biot-DA model is stable. However, in the particular case where the coefficients θ_ℓ^i, a_ℓ^i are all positive, E is an energy, and $\frac{dE}{dt} < 0$: the Biot-DA model is therefore stable in this case.

Proposition 4. *Let us assume that the abscissae θ_ℓ^i have been sorted in increasing order*

$$\theta_1^i < \theta_2^i < \cdots < \theta_N^i, \quad i = 1, 3, \tag{43}$$

and that the coefficients θ_ℓ^i, a_ℓ^i of the diffusive approximation (32) are positive. Then zero is an eigenvalue with multiplicity 6 *of* $\boldsymbol{S}$*. Moreover, the* $2\,N + 2$ *non-zero eigenvalues of* $\boldsymbol{S}$ *(denoted s_ℓ^i, $\ell = 1, \cdots, N+1$) are real positive, and satisfy*

$$0 < s_1^i < \theta_1^i + \Omega_i < \cdots < s_N^i < \theta_N^i + \Omega_i < s_{N+1}^i, \quad i = 1, 3. \tag{44}$$

Proposition 4 is proven in Appendix C. As we will see in § 4, the proposition 4 ensures the stability of the numerical method. Positivity of quadrature abscissae and weights is again the fundamental hypothesis.

3.4. Determining the Biot-DA parameters

For the sake of clarity, the space coordinates and the subscripts due to the anisotropy are omitted. The quadrature coefficients aim to approximate improper integrals of the form

$$(D + \Omega)^{1/2} w(t) = \frac{1}{\pi} \int_0^\infty \frac{1}{\sqrt{\theta}} \psi(t, \theta)\, d\theta \simeq \sum_{\ell=1}^{N} a_\ell\, \psi(t, \theta_\ell). \tag{45}$$

Moreover, the positivity of the quadrature coeffiients is crucial for the stability of the Biot-DA model and its numerical implementation, as shown in propositions 3 and 4. Two approaches can be employed for this purpose. While the most usual one is based on orthogonal polynomials, the second approach is associated with an optimization procedure applied to the viscous operators (38).

3.4.1. Gaussian quadratures

Various orthogonal polynomials exist to evaluate the improper integral (45). The first method, proposed in [15], is to use the Gauss-Laguerre quadrature formula, which approximates improper integrals over $\mathbb{R}^+$. Slow convergence of this method is explained and corrected in [16]. It consists in replacing the Gauss-Laguerre quadrature by a Gauss-Jacobi quadrature, more suitable for functions which decrease algebraically. A last improvement, proposed in [17], consists in using a modified Gauss-Jacobi quadrature formula, recasting the improper integral (45) as

$$\frac{1}{\pi}\int_0^{\infty}\frac{1}{\sqrt{\theta}}\,\psi(\theta)\,d\theta = \frac{1}{\pi}\int_{-1}^{+1}(1-\tilde{\theta})^{\gamma}(1+\tilde{\theta})^{\delta}\tilde{\psi}(\tilde{\theta})\,d\tilde{\theta} \simeq \frac{1}{\pi}\sum_{\ell=1}^{N}\tilde{a}_\ell\,\tilde{\psi}(\tilde{\theta}_\ell), \tag{46}$$

with the modified memory variable $\tilde{\psi}$ defined as

$$\tilde{\psi}(\tilde{\theta}) = \frac{4}{(1-\tilde{\theta})^{\gamma-1}(1+\tilde{\theta})^{\delta+3}}\left(\frac{1+\tilde{\theta}}{1-\tilde{\theta}}\right)\psi\left(\left(\frac{1-\tilde{\theta}}{1+\tilde{\theta}}\right)^2\right). \tag{47}$$

The abscissae $\tilde{\theta}_\ell$, which are the zeros of the Gauss-Jacobi polynomials, and the weights $\tilde{a}_\ell$ can be computed by standard routines [32]. In [17], the author proves that for fractional derivatives of order 1/2, the optimal coefficients to use are $\gamma = 1$ and $\delta = 1$. The coefficients of the diffusive approximation θ_ℓ and a_ℓ (45) are therefore related to the coefficients $\tilde{\theta}_\ell$ and $\tilde{a}_\ell$ (46) by

$$\theta_\ell = \left(\frac{1-\tilde{\theta}_\ell}{1+\tilde{\theta}_\ell}\right)^2, \quad a_\ell = \frac{1}{\pi}\,\frac{4\,\tilde{a}_\ell}{(1-\tilde{\theta}_\ell)\,(1+\tilde{\theta}_\ell)^3}. \tag{48}$$

By construction, they are strictly positive.

3.4.2. Optimization procedures

In [23, 24], we proposed a different method to determine the coefficients θ_ℓ and a_ℓ of the diffusive approximation (45). This method is based on the frequency expressions of the viscous operators and takes into account the frequency content of the source. Our requirement is therefore to approximate the viscous operator $\widehat{F^{JKD}}(\omega)$ by $\widehat{F^{DA}}(\omega)$ (38) in the frequency range of interest $I = [\omega_{\min}, \omega_{\max}]$, centered on the central angular frequency of the source. This leads to the minimization of the quantity χ^2 with respect to the abcissae θ_ℓ and to the weights a_ℓ

$$\chi^2 = \sum_{k=1}^{K}\left|\frac{\widehat{F^{DA}}(\omega_k)}{\widehat{F^{JKD}}(\omega_k)} - 1\right|^2 = \sum_{k=1}^{K}\left|\sum_{\ell=1}^{N} a_\ell\,\frac{(\Omega + j\,\omega_k)^{1/2}}{\theta_\ell + \Omega + j\,\omega_k} - 1\right|^2, \tag{49}$$

where the angular frequencies ω_k are distributed linearly in I on a logarithmic scale of K points

$$\omega_k = \omega_{\min}\left(\frac{\omega_{\max}}{\omega_{\min}}\right)^{\frac{k-1}{K-1}}, \qquad k = 1\cdots K. \tag{50}$$

In [23, 24], the abcissae θ_ℓ were arbitrarily put linearly on a logarithmic scale, as (50). Only the weights a_ℓ were optimized with a linear least-squares minimization procedure of (49). Some negative weights were obtained, which represents a major drawback, at least theoretically, since the stability of the Biot-DA model can not be guaranteed.

To remove this drawback and improve the minimization of χ^2, a nonlinear constrained optimization is developed, where both the abcissae and the weights are optimized. The coefficients θ_ℓ

and a_ℓ are now constrained to be positive. An additional constraint $\theta_\ell \leqslant \theta_{max}$ is also introduced to ensure the computational accuracy in the forthcoming numerical method (§ 4). Setting

$$\theta_\ell = (\theta'_\ell)^2, \quad a_\ell = (a'_\ell)^2, \tag{51}$$

the number of constraints decreases from $3\,N$ to N leading to the following minimization problem:

$$\min_{(\theta'_\ell, a'_\ell)} \chi^2, \quad \theta'_\ell \leqslant \sqrt{\theta_{\max}}. \tag{52}$$

The constrained minimization problem (52) is nonlinear and non-quadratic with respect to abscissae θ'_ℓ. To solve it, we implement the program SolvOpt [33, 34], used in viscoelasticity [35]. Since this Shor's algorithm is iterative, it requires an initial estimate θ'^0_ℓ, a'^0_ℓ of the coefficients which satisfies the constraints of the minimization problem (52). For this purpose, θ^0_ℓ and a^0_ℓ are initialized with the method based on the modified Gauss-Jacobi quadrature formula (48):

$$\theta'^0_\ell = \frac{1-\tilde{\theta}_\ell}{1+\tilde{\theta}_\ell}, \quad a'^0_\ell = \sqrt{\frac{1}{\pi}\,\frac{4\,\tilde{a}_\ell}{(1-\tilde{\theta}_\ell)\,(1+\tilde{\theta}_\ell)^3}}. \tag{53}$$

Different initial guess have been used, derived from Gaus-Legendre and Gauss-Jacobi methods, leading to the same final coefficients θ_ℓ and a_ℓ.

In what follows, we always use the parameters

$$\omega_{\min} = \omega_0/10, \quad \omega_{\max} = 10\,\omega_0, \quad \theta_{\max} = 100\,\omega_0, \quad K = 2\,N, \tag{54}$$

where $\omega_0 = 2\,\pi\,f_0$ is the central angular frequency of the source.

3.4.3. Discussion

To compare the quadrature methods presented in § 3.4.1 and 3.4.2, we first define the error of model ε_{mod} as

$$\varepsilon_{mod} = \left\| \frac{\widehat{F}^{DA}(\omega)}{\widehat{F}^{JKD}(\omega)} - 1 \right\|_{L_2} = \left(\int_{\omega_{\min}}^{\omega_{\max}} \left| \frac{\widehat{F}^{DA}(\omega)}{\widehat{F}^{JKD}(\omega)} - 1 \right|^2 d\omega \right)^{1/2}. \tag{55}$$

The variation of ε_{mod} in terms of the number N of memory variables, for $f_0 = 200$ kHz and $f_c = 3.84$ kHz, is represented on figure 2-a. The Gauss-Jacobi method converges very slowly, and the error is always larger than 1 % even for $N = 50$. Moreover, for values of $N \leqslant 10$, the error is always larger than 60 %. For both the linear and the nonlinear optimizations, the errors decrease rapidly with N. Nevertheless, the nonlinear procedure outperforms the results obtained in the linear case. For $N = 8$ for instance, the relative error of the nonlinear optimization ($\varepsilon_{mod} \simeq 7.16\,10^{-3}$ %) is 514 times smaller that the error of the linear optimization ($\varepsilon_{mod} \simeq 3.68$ %). For larger values of N, the system is poorly conditioned and the order of convergence deteriorates; in practice, this is not penalizing since large values of N are not used. An example of a priori parametric determination of N in terms of both the frequency range and the desired accuracy is also given in figure 2-b for the nonlinear procedure. The case $N = 0$ corresponds to the Biot-LF model.

It is also important to compare the influence of the quadrature coefficient on the physical observables. For that purpose, we represent on figure 3 the phase velocity and the attenuation of the

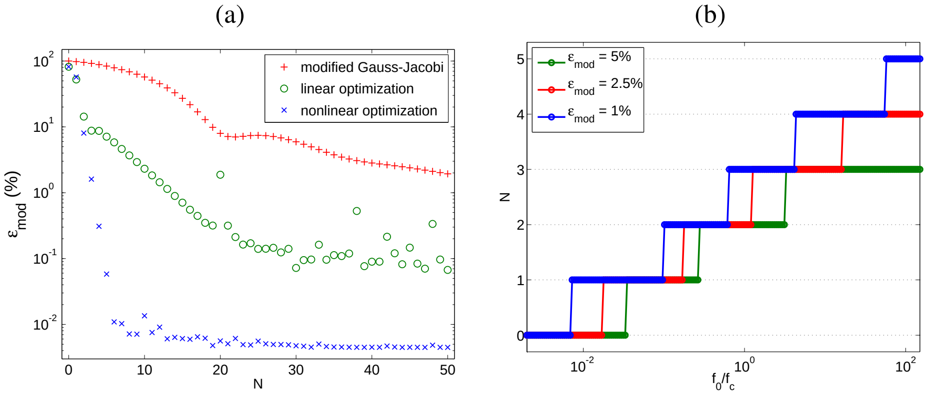

Figure 2: (a): relative error ε_{mod} in terms of N for both the modified Gauss-Jacobi quadrature and the nonlinear constrained optimization. (b): required values of N in terms of f_0/f_{c1} and the required accuracy ε_{mod} for the nonlinear optimization.

slow wave of the Biot-DA model, obtained with the different quadrature methods. As expected, the results given by the Gauss-Jacobi method are extremely poor. On the contrary, the linear and non-linear procedures are able to represent very accurately the variations of these quantities on the considered range of frequencies, even for small values of N. Based on these results and the positivity requirement, the nonlinear constrained optimization is therefore considered as the better way to determine the coefficients of the diffusive approximation. This method is used in all what follows.

4. Numerical modeling

4.1. Splitting

In order to integrate the Biot-DA system (37), a uniform grid is introduced, with mesh size Δx,, Δz and time step Δt. The approximation of the exact solution $\boldsymbol{U}(x_i = i\,\Delta x, z_j = j\,\Delta z, t_n = n\,\Delta t)$ is denoted by $\boldsymbol{U}_{ij}^n$, with $0 \leqslant i \leqslant N_x$, $0 \leqslant j \leqslant N_z$. If $\Delta x = \Delta z$, a straightforward discretization of (37) by an explicit time scheme typically leads to the following condition of stability

$$\Delta t \leqslant \min\left(\Upsilon \frac{\Delta x}{\max\limits_{\varphi\in[0,\pi/2]} c_{pf}^{\infty}(\varphi)}, \frac{2}{R(\boldsymbol{S})}\right), \tag{56}$$

where $R(\boldsymbol{S})$ is the spectral radius of $\boldsymbol{S}$, and $\Upsilon > 0$ is obtained by a Von-Neumann analysis when $\boldsymbol{S} = \boldsymbol{0}$. The first term of (56), which depends of the propagation matrices $\boldsymbol{A}$ and $\boldsymbol{B}$, is the classical CFL condition. The second term of (56) depends only on the diffusive matrix $\boldsymbol{S}$. From proposition 4, we deduce that the spectral radius of $\boldsymbol{S}$ satisfies

$$R(\boldsymbol{S}) > \max_{\ell=1,\cdots,N}(\theta_\ell^1 + \Omega_1, \theta_\ell^3 + \Omega_3) \tag{57}$$

if the coefficients θ_ℓ^i and a_ℓ^i of the diffusive approximation are positive. With highly dissipative fluids, the second term of (56) can be so small that numerical computations are intractable.

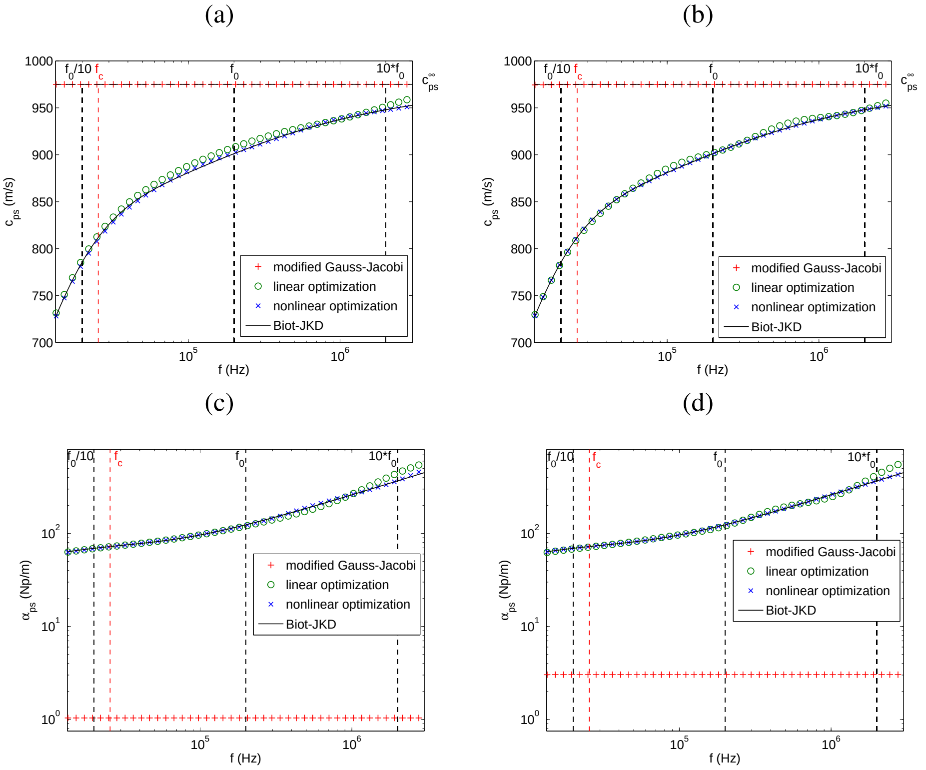
(a) (b)

(c) (d)

Figure 3: phase velocity (a), (b) and attenuation (c), (d) of the slow quasi-compressional wave. Comparison between the Biot-DA model and the Biot-JKD model. Left: $N = 3$, right: $N = 6$.

A more efficient strategy is adopted here, based on the second-order Strang splitting [36]. It consists in splitting the original system (37) into a propagative part

$$\frac{\partial \boldsymbol{U}}{\partial t} + \boldsymbol{A}\,\frac{\partial \boldsymbol{U}}{\partial x} + \boldsymbol{B}\,\frac{\partial \boldsymbol{U}}{\partial z} = \boldsymbol{0}, \qquad (\boldsymbol{H}_p) \tag{58}$$

and a diffusive part with forcing

$$\frac{\partial \boldsymbol{U}}{\partial t} = -\boldsymbol{S}\,\boldsymbol{U} + \boldsymbol{G}, \qquad (\boldsymbol{H}_d) \tag{59}$$

where $\boldsymbol{H}_p$ and $\boldsymbol{H}_d$ are the operators associated with each part. One solves alternatively the propagative part and the diffusive part:

$$\boldsymbol{U}^{n+1} = \boldsymbol{H}_d\left(t_{n+1}, \frac{\Delta t}{2}\right) \circ \boldsymbol{H}_p(\Delta t) \circ \boldsymbol{H}_d\left(t_n, \frac{\Delta t}{2}\right) \boldsymbol{U}^n. \tag{60}$$

The discrete operator $\boldsymbol{H}_p$ associated with the propagative part (58) is an ADER 4 (Arbitrary DERivatives) scheme [37]. This scheme is fourth-order accurate in space and time, is dispersive of order 4 and dissipative of order 6 [38], and has a stability limit $\Upsilon = 1$. On Cartesian grids, ADER 4 amounts to a fourth-order Lax-Wendroff scheme.

The solution of (59) is given by

$$\begin{aligned} \boldsymbol{H}_d\left(t_k, \frac{\Delta t}{2}\right) \boldsymbol{U}(t_0) &= e^{-\boldsymbol{S}\,\Delta t/2}\,\boldsymbol{U}\,(t_0) + \int_{t_0}^{t_0+\Delta t/2} e^{-\boldsymbol{S}\,(t_0+\Delta t/2-\tau)}\,\boldsymbol{G}(\tau)\,d\tau, \\ &\simeq e^{-\boldsymbol{S}\,\frac{\Delta t}{2}}\,\boldsymbol{U}(t_0) - (\boldsymbol{I} - e^{-\boldsymbol{S}\,\frac{\Delta t}{2}})\,\boldsymbol{S}^{-1}\,\boldsymbol{G}(t_k), \end{aligned} \tag{61}$$

with $k = n$ or $n+1$. The exponential matrix $e^{-\boldsymbol{S}\,\Delta t/2}$ is computed numerically using the $(6,6)$ Padé approximation in the "scaling and squaring method" [39]. Proposition 4 ensures that the numerical integration of the diffusive step (59) is unconditionally stable [23]. Without forcing, i.e. $\boldsymbol{G} = \boldsymbol{0}$, the integration of the diffusive part (59) is exact.

The full algorithm is therefore stable under the optimum CFL condition of stability

$$\Delta t = \Upsilon\,\frac{\Delta x}{\max\limits_{\varphi\in[0,\pi/2]} c_{pf}^{\infty}(\varphi)}, \qquad \Upsilon \leqslant 1, \tag{62}$$

which is always independent of the Biot-DA model coefficients. Since the matrices $\boldsymbol{A}$, $\boldsymbol{B}$ and $\boldsymbol{S}$ do not commute, the order of convergence decreases from 4 to 2. Using a fourth-order ADER scheme is nevertheless advantageous, compared with the second-order Lax-Wendroff scheme: the stability limit is improved, and numerical artifacts (dispersion, attenuation, anisotropy) are greatly reduced.

4.2. Immersed interface method

Let us consider two transversely isotropic homogeneous poroelastic media Ω_0 and Ω_1 separated by a stationary interface Γ, as shown in figure 4. The governing equations (37) in each medium have to be completed by a set of jump conditions. The simple case of perfect bonding and perfect hydraulic contact along Γ is considered here, modeled by the jump conditions [40]:

$$[\boldsymbol{v}_s] = \boldsymbol{0}, \quad [\boldsymbol{w}.\boldsymbol{n}] = 0, \quad \left[\underline{\boldsymbol{\sigma}}.\boldsymbol{n}\right] = \boldsymbol{0}, \quad [p] = 0. \tag{63}$$

Figure 4: interface Γ between two poroelastic media Ω_0 and Ω_1.

The discretization of the interface conditions requires special care. A straightforward stair-step representation of interfaces introduces first-order geometrical errors and yields spurious numerical diffractions. In addition, the jump conditions (63) are not enforced numerically if no special treatment is applied. Lastly, the smoothness requirements to solve (58) are not satisfied, decreasing the convergence rate of the ADER scheme.

To remove these drawbacks while maintaining the efficiency of Cartesian grid methods, immersed interface methods constitute a possible strategy [41, 42, 11]. The latter studies can be consulted for a detailed description of this method. The basic principle is as follows: at the irregular nodes where the ADER scheme crosses an interface, modified values of the solution are used on the other side of the interface instead of the usual numerical values.

Calculating these modified values is a complex task involving high-order derivation of jump conditions (63), high-order derivation of the Beltrami-Michell equation (8) and algebraic manipulation, such as singular value decompositions. All these time consuming procedures can be carried out during a preprocessing stage and only small matrix-vector multiplications need to be performed during the simulation. After optimizing the code, the extra CPU cost can be practically negligible, i.e. lower than 1% of that required by the time-marching procedure.

Compared with § 3-3 of [11], the modifications induced by anisotropy concern

- step 1: the derivation of the jump conditions,
- step 2: the derivation of the Beltrami-Michell equation.

These modifications are tedious and hence will not be repeated here. They are straightforwardly deduced from the new expressions (8) and (34).

5. Numerical experiments

Configuration

In order to demonstrate the ability of the present method to be applied to a wide range of applications, the numerical tests will be run on two different transversely isotropic porous media. The medium Ω_0 is composed of thin layers of epoxy and glass, strongly anisotropic if the wavelengths are large compared to the thick of the layers [18]. The medium Ω_1 is water saturated Berea sandstone, which is sedimentary rock commonly encountered in petroleum engineering. The grains are predominantly sand sized and composed of quartz bonded by silica [18, 43].

The values of the physical parameters are given in table 1. The viscous characteristic lengths Λ_1 and Λ_3 are obtained by setting the Pride numbers $P_1 = P_3 = 0.5$. We also report in these tables some useful values, such as phase velocities, critical frequencies, and quadrature parameters computed for each media. The central frequency of the source is $f_0 = 200$ kHz, and the quadrature coefficients θ_ℓ^i, a_ℓ^i, $i = 1, 3$, are determined by nonlinear constrained optimization with $N = 3$ memory variables. The error of model ε_{mod} (55) is also given. We note that the transition frequencies f_{c1} and f_{c3} are the same for both Ω_0 and Ω_1. In this particular case, the coefficients of the diffusive approximation are therefore also the same. In all the numerical simulations, the time step is computed from the physical parameters of the media through relations (62), setting the CFL number $\Upsilon = 0.95$. The numerical experiments are performed on an Intel Core i7 processor at 2.80 GHz.

In the first test, the computational domain $[-0.15, 0.15]^2$ m is discretized with $N_x = N_z = 2250$ grid nodes in each direction, which amounts to 20 points per slow compressional wavelength in Ω_0. In the other tests, the computational domain is discretized with $N_x = N_z = 1500$, which amounts also to 20 points per slow compressional wavelength in Ω_0 and in Ω_1.

Test 1: homogeneous medium

In the first test, the homogeneous medium Ω_0 (table 1) is excited by a source point located at (0 m, 0 m). The only non-null component of the forcing $\boldsymbol{F}$ (36) is $G_{\sigma_{13}} = g(t)\, h(x, z)$, where $g(t)$ is a Ricker signal of central frequency f_0 and of time-shift $t_0 = 2/f_0 = 10^{-5}$ s:

$$g(t) = \begin{cases} \left(2\,\pi^2 f_0^2 \left(t - \dfrac{1}{f_0}\right)^2 - 1\right) \exp\left(-\pi^2 f_0^2\, (t - \dfrac{1}{f_0})^2\right) & \text{if } 0 \leqslant t \leqslant t_0, \\ 0 & \text{otherwise,} \end{cases} \tag{64}$$

and $h(x, z)$ is a truncated Gaussian centered at point $(0, 0)$, of radius $R_0 = 6.56\,10^{-3}$ m and $\Sigma = 3.28\,10^{-3}$ m:

$$h(x, z) = \begin{cases} \dfrac{1}{\pi\,\Sigma^2} \exp\left(-\dfrac{x^2 + z^2}{\Sigma^2}\right) & \text{if } 0 \leqslant x^2 + z^2 \leqslant R_0^2, \\ 0 & \text{otherwise.} \end{cases} \tag{65}$$

We use a truncated gaussian for $h(x, z)$ rather than a Dirac distribution to avoid spurious numerical artifacts localized around the source point. This source generates cylindrical waves of all types: fast and slow quasi-compressional waves and quasi-shear waves, which are denoted by qP_f, qP_s and qS, respectively, in figure 5. The three waves are observed in the pressure field. Comparison with the theoretical wavefront, represented by a black dotted line in figure 5, shows that the computed waves are well positionned at this instant ($t_1 \simeq 2.72\,10^{-5}$ s). No special care is applied to simulate outgoing waves (with PML, for instance), since the simulation is stopped before the waves have reached the edges of the computational domain. The cusp of the shear wave is seen in the numerical solution.

Test 2: diffraction of a plane wave by a plane interface

In all the following tests, the source is a plane right-going fast compressional wave, whose wavevector $\boldsymbol{k}$ makes an angle $\theta = 0$ degree with the horizontal x-axis. Its time evolution is the same Ricker signal as in the first test (64). We use periodic boundary conditions at the top and at the bottom of the domain.

In the second test, the validity of the method is checked in the particular case of heterogeneous transversely isotropic media, where a semi-analytical solution can be obtained easily. The

	Parameters	Ω_0	Ω_1
Saturating fluid	ρ_f (kg/m^3)	1040	1040
	η (Pa.s)	10^{-3}	10^{-3}
	K_f (GPa)	2.5	2.5
Grain	ρ_s (kg/m^3)	1815	2500
	K_s (GPa)	40	80
Matrix	ϕ	0.2	0.2
	$\mathcal{T}_1$	2	2
	$\mathcal{T}_3$	3.6	3.6
	κ_1 (m^2)	$6.\ 10^{-13}$	$6.\ 10^{-13}$
	κ_3 (m^2)	10^{-13}	10^{-13}
	c_{11} (GPa)	39.4	71.8
	c_{12} (GPa)	1	3.2
	c_{13} (GPa)	5.8	1.2
	c_{33} (GPa)	13.1	53.4
	c_{55} (GPa)	3	26.1
	Λ_1 (m)	$6.93\ 10^{-6}$	$2.19\ 10^{-7}$
	Λ_3 (m)	$3.79\ 10^{-6}$	$1.20\ 10^{-7}$
Dispersion	$c_{pf}^{\infty}(0)$ (m/s)	5244.40	6004.31
	$c_{pf}(f_0, 0)$ kHz (m/s)	5227.10	5988.50
	$c_{pf}^{\infty}(\pi/2)$ (m/s)	3583.24	5256.03
	$c_{pf}(f_0, \pi/2)$ (m/s)	3581.42	5245.84
	$c_{ps}^{\infty}(0)$ (m/s)	975.02	1026.45
	$c_{ps}(f_0, 0)$ (m/s)	901.15	949.33
	$c_{ps}^{\infty}(\pi/2)$ (m/s)	604.41	745.59
	$c_{ps}(f_0, \pi/2)$ (m/s)	534.88	661.32
	$c_{s}^{\infty}(0)$ (m/s)	1368.36	3484.00
	$c_{s}(f_0, 0)$ (m/s)	1361.22	3470.45
	$c_{s}^{\infty}(\pi/2)$ (m/s)	1388.53	3522.07
	$c_{s}(f_0, \pi/2)$ (m/s)	1381.07	3508.05
	f_{c1} (Hz)	$2.55\ 10^4$	$2.55\ 10^4$
	f_{c3} (Hz)	$8.50\ 10^4$	$8.50\ 10^4$
Optimization	θ_1^1 (rad/s)	$1.64\ 10^5$	$1.64\ 10^5$
	θ_2^1 (rad/s)	$2.80\ 10^6$	$2.80\ 10^6$
	θ_3^1 (rad/s)	$3.58\ 10^7$	$3.58\ 10^7$
	a_1^1 (rad$^{1/2}$/s$^{1/2}$)	$5.58\ 10^2$	$5.58\ 10^2$
	a_2^1 (rad$^{1/2}$/s$^{1/2}$)	$1.21\ 10^3$	$1.21\ 10^3$
	a_3^1 (rad$^{1/2}$/s$^{1/2}$)	$7.32\ 10^3$	$7.32\ 10^3$
	ε_{mod}^1 (%)	1.61	1.61
	θ_1^3 (rad/s)	$3.14\ 10^5$	$3.14\ 10^5$
	θ_2^3 (rad/s)	$5.06\ 10^7$	$5.06\ 10^7$
	θ_3^3 (rad/s)	$4.50\ 10^6$	$4.50\ 10^6$
	a_1^3 (rad$^{1/2}$/s$^{1/2}$)	$7.57\ 10^2$	$7.57\ 10^2$
	a_2^3 (rad$^{1/2}$/s$^{1/2}$)	$8.79\ 10^3$	$8.79\ 10^3$
	a_3^3 (rad$^{1/2}$/s$^{1/2}$)	$1.38\ 10^3$	$1.38\ 10^3$
	ε_{mod}^3 (%)	0.53	0.53

Table 1: Physical parameters of the transversely isotropic media used in the numerical experiments. The phase velocities $c_{pf}(f_0, \varphi)$, $c_{ps}(f_0, \varphi)$ and $c_s(f_0, \varphi)$ are computed at $f = f_0 = 200$ kHz when the wavevector $\boldsymbol{k}$ makes an angle φ with the horizontal x-axis, and $c_{pf}^{\infty}(\varphi)$, $c_{ps}^{\infty}(\varphi)$, $c_{s}^{\infty}(\varphi)$ denote the high-frequency limit of the phases velocities.

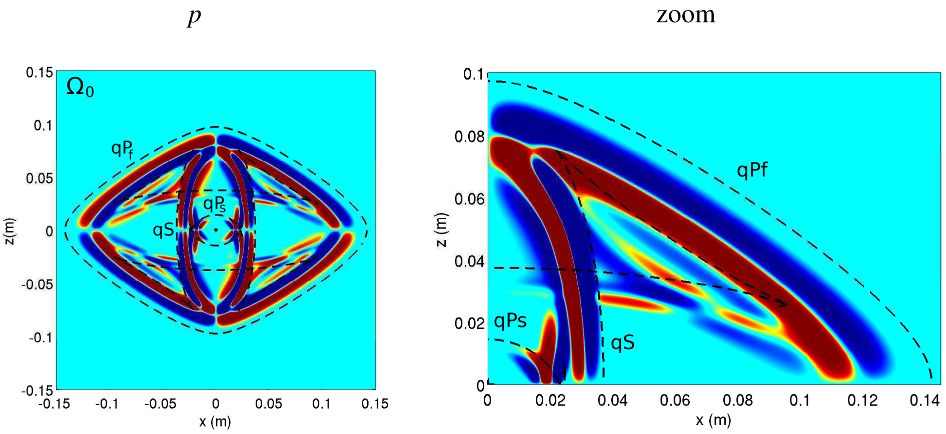

p

zoom

Figure 5: test 1. Fast and slow quasi-compressional waves, respectively qP_f and qP_s, and quasi-shear wave qS emitted by a source point at (0 m, 0 m). Pressure at $t_1 \simeq 2.72\,10^{-5}$ s.

media Ω_0 and Ω_1 are separated by a vertical wave plane interface at $x = 0$ m. The incident P_f-wave (Ip_f) propagates in the medium Ω_1. The figure 6 shows a snapshot of the pressure at $t_1 \simeq 1.48\,10^{-5}$ s, on the whole computational domain. The reflected fast and slow quasi-compressional waves, denoted respectively Rp_f and Rp_s, propagate in the medium Ω_1; and the transmitted fast and slow quasi-compressional waves, denoted respectively Tp_f and Tp_s, propagate in the medium Ω_0. In this case, we compute the exact solution of Biot-DA thanks to standard tools of Fourier analysis. The figure 7 shows the excellent agreement between the analytical and the numerical values of the pressure along the line $z = 0$ m. Despite the relative simplicity of

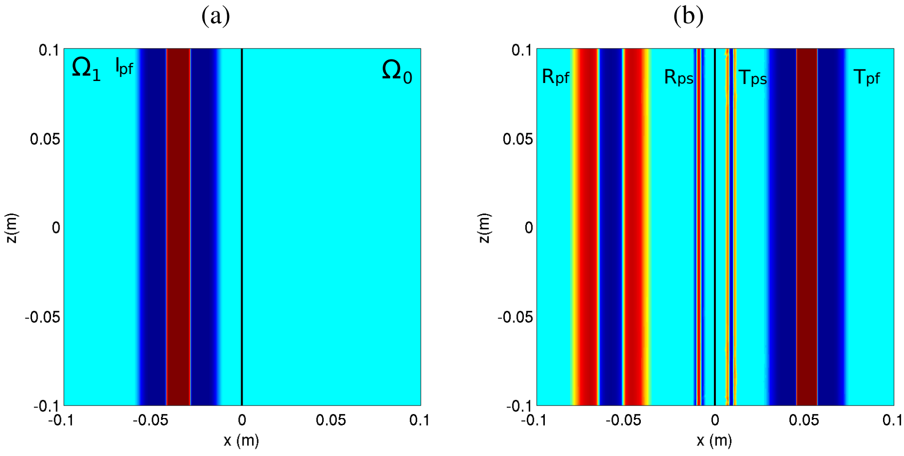

(a)

(b)

Figure 6: test 2. Snapshot of pressure at initial time (a) and at $t_1 \simeq 1.48\,10^{-5}$ s (b). The plane interface is denoted by a straight black line, separating Ω_1 (on the left) and Ω_0 (on the right).

this configuration (1D evolution of the waves and lack of shear waves), it can be viewed as a validation of the numerical method which is fully 2D whatever the geometrical setting.

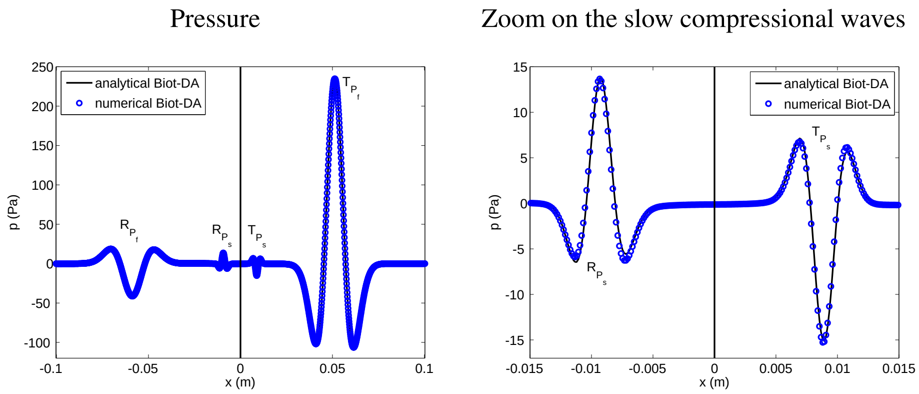

Pressure

Zoom on the slow compressional waves

Figure 7: test2. Pressure along the line $z = 0$ m; vertical line denotes the interface. Comparison between the numerical values (circle) and the analytical values (solid line) of p at $t_1 \simeq 1.48\,10^{-5}$ s.

Test 3: diffraction of a plane wave by cylinders

In the previous test, the interface was plane, but more complex geometries can be handled on a Cartesian grid thanks to the immersed interface method. As an example, we simulate the interaction of a plane wave with a cylindrical scatterer filled by medium Ω_1, and immersed in medium Ω_0. The cylinder, of radius 0.015 m, is centered at point (0.01 m, 0 m). The incident plane wave propagates in the medium Ω_0. The initial conditions are illustrated in figure 8-(a), while the snapshot of p at time $t_1 \simeq 1.69\,10^{-5}$ s is represented on figure 8-(b). Classical waves conversions and scattering phenomena are observed. Since the phase velocity c_{pf} in the medium Ω_1 is greater than in the medium Ω_0, the transmitted fast compressional wave has a curved wavefront. Moreover, the shape of the reflected waves illustrates the anisotropy of the medium Ω_0.

Test 4: multiple ellipsoidal scatterers

To illustrate the ability of the proposed numerical strategy to handle even more complex geometries, 200 ellipsoidal scatterers of medium Ω_1, with major and minor radii of 0.025 m and 0.02 m, are randomly distributed in a matrix of medium Ω_0, leading to a concentration of 25 %. The pressure is represented at the initial time on figure 9 and at time $t_1 \simeq 1.43\,10^{-4}$ s on figure 10. This simulation has taken approximately 11.5 h of preprocessing and 8.5 h of time-stepping. Similar numerical experiments are also performed for a concentration of scatterer of 10 % and 15 %.

At each time step, the components of $\boldsymbol{U}_{ij}^n$ are stored inside the subdomain containing the inclusions. For this purpose, a uniform network consisting of $N_l = 800$ lines and $N_c = 25$ columns of receivers is put in the subdomain. The position of the receivers is given by (x_i, z_j), where $i = 0, \cdots, N_c - 1$ and $j = 0, \cdots, N_l - 1$. The field $\boldsymbol{U}_{ij}^n$ recorded on each array (each line of receivers), represented on figure 11-a, corresponds to a field propagating along one horizontal line of receivers. A main wave train is clearly visible, followed by a coda. Summing the time

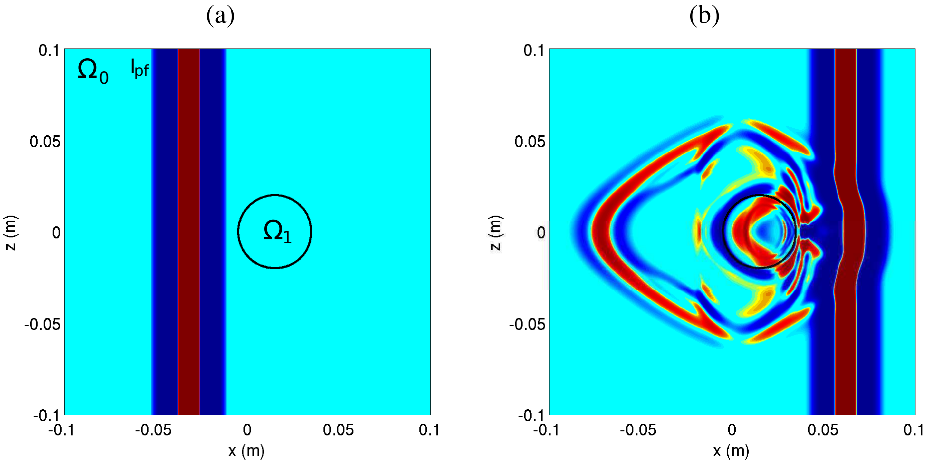

Figure 8: test 3. Snapshot of pressure at initial time (a) and at $t_1 \simeq 1.69\,10^{-5}$ s (b). The cylinder is denoted by a black circle, separating the porous media Ω_0 (outside) and Ω_1 (inside).

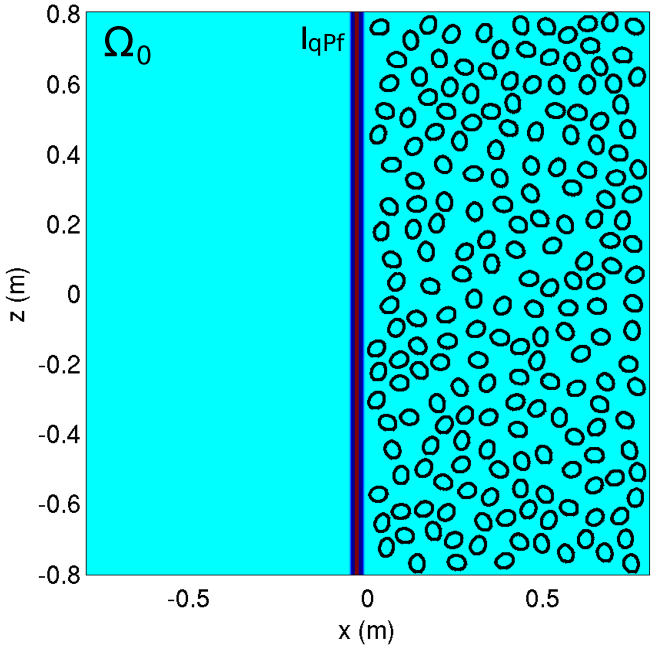

Figure 9: test 4. Multiple scattering in random media. Snapshot of p at the initial time. The matrix is Ω_0, whereas the 200 scatterers are Ω_1.

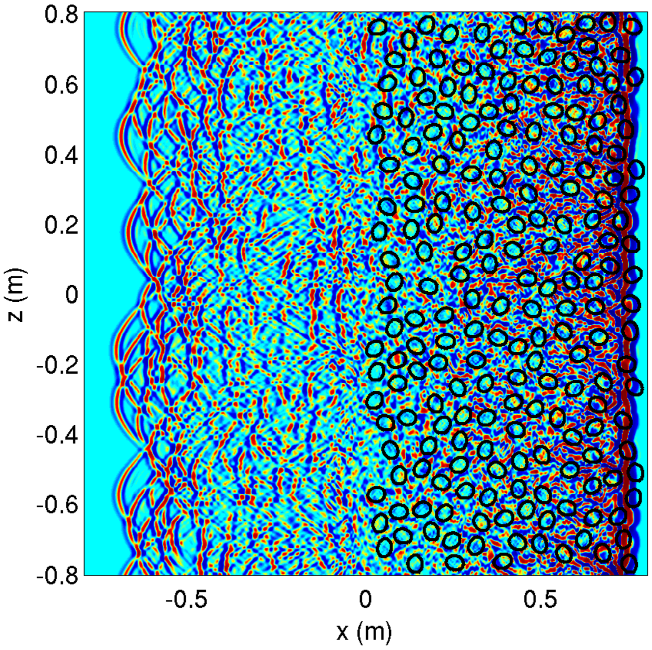

Figure 10: test 4. Multiple scattering in random media. Snapshot of p at time $t_1 \simeq 1.43\ 10^{-4}$ s. The matrix is Ω_0, whereas the 200 scatterers are Ω_1.

histories of these N_c arrays gives a coherent field propagating in the x direction:

$$\overline{\boldsymbol{U}}_i^n = \frac{1}{N_l}\sum_{j=0}^{N_l-1}\boldsymbol{U}_{ij}^n. \tag{66}$$

On the coherent seismogram thus obtained, represented on figure 11-b, the coda has disappeared, and the main wave train behaves like a plane wave propagating in a homogeneous (but dispersive and attenuating) medium. The coherent phase velocity $c(\omega)$, represented in figure 12-a, is computed by applying a $\mathfrak{p}-\omega$ transform to the space-time data on the coherent field (66), where $\mathfrak{p} = 1/c$ is the slowness of the waves [44, 45]. The horizontal lines represent a simple average of the phase velocities weighted by the concentration. The coherent attenuation $\alpha(\omega)$ is estimated from the decrease in the amplitude spectrum of the coherent field during the propagation of the waves, see 12-b. An error estimate is also deduced, represented in figure 12 by vertical lines.

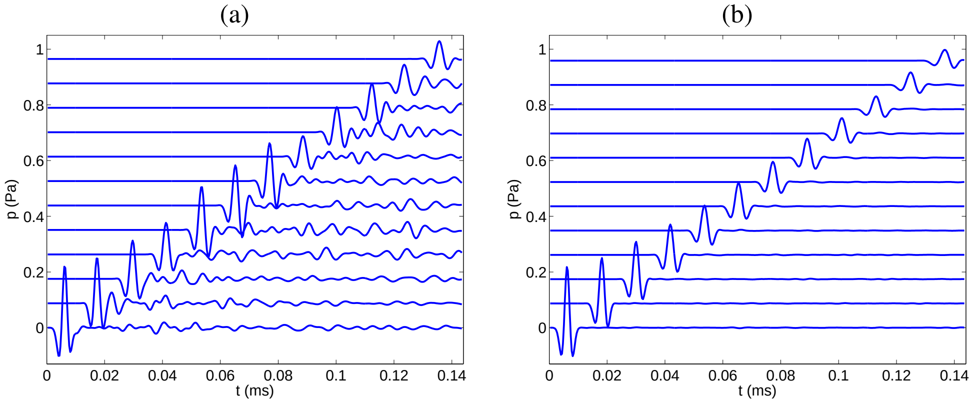

Figure 11: test 4. Incident plane qP_s-wave in a medium with 25% inclusion concentration. (a): pressure recorded along an array, (b): coherent pressure obtained afer summation.

6. Conclusion

An explicit finite-difference method has been developed here to simulate transient poroelastic waves in the full range of validity of the Biot-JKD model, which involves order $1/2$ fractional derivatives. A diffusive representation transforms the fractional derivatives, non-local in time, into a continuum of local problems, approximated by quadrature formulae. The Biot-JKD model is then replaced by an approximate Biot-DA model, much more tractable numerically. The coefficients of the diffusive approximation are determined by a nonlinear constrained optimization procedure, leading to a small number of memory variables. The hyperbolic Biot-DA system of partial differential equations is discretized using various tools of scientific computing: Strang splitting, fourth-order ADER scheme, immersed interface method. It enables to treat efficiently and accurately the propagation of transient waves in transversely isotropic porous media.

Some future lines of research are suggested:

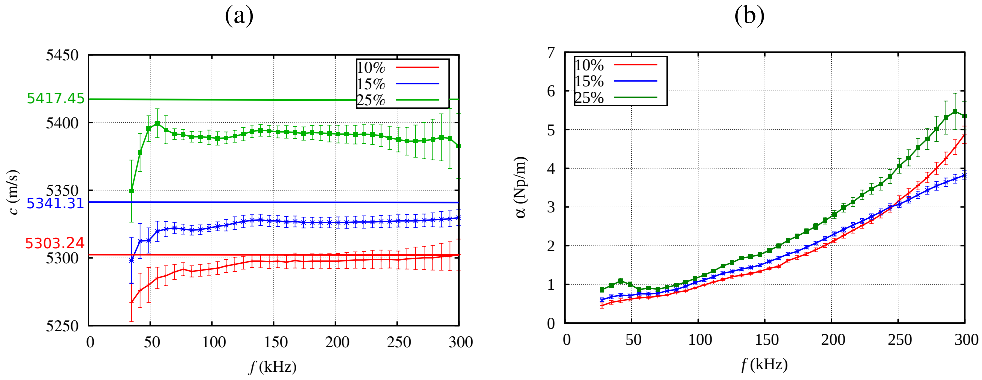

Figure 12: test 4. Effective phase velocity (a) and effective attenuation (b) at various inclusion concentrations. The vertical lines represents the error bars. The horizontal lines in (a) give the average phase velocity weighted by the concentration.

- *Multiple scattering.* Many theoretical methods of multiple scattering have been developed to determine the effective wavenumber of media with random scatterers; see for instance the Independent Scattering Approximation and the Waterman-Truell method [46]. The main drawback of these methods is that their validity is restricted to small concentrations of scatterers, typically less than 10 %. On the contrary, numerical methods do not suffer from such a limitation if suitable efforts are done. In particular, the errors due to the discretization (numerical dispersion, numerical dissipation, spurious diffractions on interfaces, ...) must be much smaller than the physical quantities of interest. In [47], numerical simulations were used in the elastic case to estimate the accuracy of standard theoretical models, and also to show the improvement induced by recent models of multiple scattering [48]. As shown in test 4 of § 5, the numerical tools presented here make possible a similar study poroelastic random media and comparisons with theoretical models [49, 50].

  However, realistic configurations would involve approximately 1500 scatterers, and sizing of the experiments leads to $N_x \times N_z = 10000^2$, and 10000 time iterations are required. Consequently, the numerical method has to be parallelized, for instance by Message Passing Interface (MPI).

- *Thermic boundary-layer.* In cases where the saturating fluid is a gas, the effects of thermal expansion of both pore fluid and the matrix have to be taken into account. In the HF regime, the thermal exchanges between fluid and solid phase occur in a small layer close to the surface of the pores. In this case, the dynamic thermal permeability is introduced [51], leading in the time-domain to an additional shifted fractional derivative of order $1/2$. The numerical method developed in this paper can be applied without difficulty by introducing additional memory variables.

- *Fractional derivatives in space.* The Biot theory is very efficient to predict the macroscopic behavior of long-wavelength sound propagation in porous medium with relatively simple microgeometries. However, it remains far to describe correctly the coarse-grained dynamics of the medium when the microgeometry of the porous medium become more complex, for instance fractal. For rigid-framed porous media permeated by a viscothermal fluid, a generalized macroscopic nonlocal theory of sound propagation has been developed to take into account not only temporal dispersion, but also spatial dispersion [52]. In this case, the coefficients depends on the frequency and on the wavenumber. In the space-time domain, it introduces not only time-fractional derivatives, but also space-fractional derivatives. Numerical modeling of space-fractional differential equations has been addressed by several authors [53, 54], by using a Grünwald-Letnikov approximation. The diffusive approximation of such derivatives constitutes an interesting challenge.

Acknowledgments

The authors wish to thank Dr Mathieu Chekroun (LAUM, France) for his insights about multiple scattering and for computing the coherent phase velocity and attenuation with the $\mathfrak{p}-\omega$ transform in test 4.

Appendix A. Proof of proposition 1

The equation (10a) is multiplied by ${\boldsymbol{v}_s}^T$ and integrated

$$\int_{\mathbb{R}^2}\left(\rho\,{\boldsymbol{v}_s}^T\,\frac{\partial\boldsymbol{v}_s}{\partial t}+\rho_f\,{\boldsymbol{v}_s}^T\,\frac{\partial\boldsymbol{w}}{\partial t}-{\boldsymbol{v}_s}^T\,(\nabla.\underline{\boldsymbol{\sigma}})\right)dx\,dz=0. \tag{A.1}$$

The first term in (A.1) is written

$$\int_{\mathbb{R}^2}\rho\,{\boldsymbol{v}_s}^T\,\frac{\partial\boldsymbol{v}_s}{\partial t}\,dx\,dz=\frac{d}{dt}\,\frac{1}{2}\int_{\mathbb{R}^2}\rho\,{\boldsymbol{v}_s}^T\,\boldsymbol{v}_s\,dx\,dz. \tag{A.2}$$

Integrating by part and using (7), we obtain

$$\begin{aligned}
-\int_{\mathbb{R}^2}{\boldsymbol{v}_s}^T\,(\nabla.\underline{\boldsymbol{\sigma}})\,dx\,dz &= \int_{\mathbb{R}^2}\boldsymbol{\sigma}^T\,\frac{\partial\boldsymbol{\varepsilon}}{\partial t}\,dx\,dz,\\
&= \int_{\mathbb{R}^2}\boldsymbol{\sigma}^T\left(\boldsymbol{C}^{-1}\,\frac{\partial\boldsymbol{\sigma}}{\partial t}-\boldsymbol{C}^{-1}\boldsymbol{\beta}\,\frac{\partial p}{\partial t}\right)dx\,dz,\\
&= \frac{d}{dt}\,\frac{1}{2}\int_{\mathbb{R}^2}\boldsymbol{\sigma}^T\,\boldsymbol{C}^{-1}\,\boldsymbol{\sigma}\,dx\,dz+\int_{\mathbb{R}^2}\boldsymbol{\sigma}^T\,\boldsymbol{C}^{-1}\,\boldsymbol{\beta}\,\frac{\partial p}{\partial t}\,dx\,dz,\\
&= \frac{d}{dt}\,\frac{1}{2}\int_{\mathbb{R}^2}\left(\boldsymbol{\sigma}^T\,\boldsymbol{C}^{-1}\,\boldsymbol{\sigma}+2\,\boldsymbol{\sigma}^T\,\boldsymbol{C}^{-1}\,\boldsymbol{\beta}\,p\right)dx\,dz-\int_{\mathbb{R}^2}\left(\frac{\partial\boldsymbol{\sigma}}{\partial t}\right)^T\boldsymbol{C}^{-1}\,\boldsymbol{\beta}\,p\,dx\,dz.
\end{aligned} \tag{A.3}$$

Equation (10b) is multiplied by $\boldsymbol{w}^T$ and integrated

$$\begin{aligned}
&\int_{\mathbb{R}^2}\left\{\rho_f\,\boldsymbol{w}^T\,\frac{\partial\boldsymbol{v}_s}{\partial t}+\boldsymbol{w}^T\,\mathrm{diag}\,(\rho_{wi})\,\frac{\partial\boldsymbol{w}}{\partial t}+\boldsymbol{w}^T\,\nabla p\right.\\
&\left.+\boldsymbol{w}^T\,\mathrm{diag}\left(\tfrac{\eta}{\kappa_i}\,\tfrac{1}{\Omega_i}\,(D+\Omega_i)^{1/2}\right)\boldsymbol{w}\right\}dx\,dz=0.
\end{aligned} \tag{A.4}$$

The second term in (A.4) can be written

$$\int_{\mathbb{R}^2}\boldsymbol{w}^T\,\mathrm{diag}\,(\rho_{wi})\,\frac{\partial\boldsymbol{w}}{\partial t}\,dx\,dz=\frac{d}{dt}\,\frac{1}{2}\int_{\mathbb{R}^2}\boldsymbol{w}^T\,\mathrm{diag}\,(\rho_{wi})\,\boldsymbol{w}\,dx\,dz. \tag{A.5}$$

Integrating by part the third term of (A.4), we obtain

$$\begin{aligned}
&\int_{\mathbb{R}^2} \boldsymbol{w}^T\,\nabla p\,dx\,dz = -\int_{\mathbb{R}^2} p\,\nabla.\boldsymbol{w}\,dx\,dz,\\
&= \int_{\mathbb{R}^2} p\,\frac{\partial \xi}{\partial t}\,dx\,dz,\\
&= \int_{\mathbb{R}^2} p\left(\frac{1}{m}\,\frac{\partial p}{\partial t} + \boldsymbol{\beta}^T\,\frac{\partial \boldsymbol{\varepsilon}}{\partial t}\right)dx\,dz,\\
&= \frac{d}{dt}\,\frac{1}{2}\int_{\mathbb{R}^2}\frac{1}{m}\,p^2\,dx\,dz + \int_{\mathbb{R}^2} p\,\boldsymbol{\beta}^T\left(\boldsymbol{C}^{-1}\,\frac{\partial \boldsymbol{\sigma}}{\partial t} + \boldsymbol{C}^{-1}\,\boldsymbol{\beta}\,\frac{\partial p}{\partial t}\right)dx\,dz,\\
&= \frac{d}{dt}\,\frac{1}{2}\int_{\mathbb{R}^2}\frac{1}{m}\,p^2\,dx\,dz + \int_{\mathbb{R}^2}\boldsymbol{\beta}^T\,\boldsymbol{C}^{-1}\,\frac{\partial \boldsymbol{\sigma}}{\partial t}\,p\,dx\,dz + \int_{\mathbb{R}^2}\boldsymbol{\beta}^T\,\boldsymbol{C}^{-1}\,\boldsymbol{\beta}\,p\,\frac{\partial p}{\partial t}\,dx\,dz,\\
&= \frac{d}{dt}\,\frac{1}{2}\int_{\mathbb{R}^2}\frac{1}{m}\,p^2\,dx\,dz + \int_{\mathbb{R}^2}\boldsymbol{\beta}^T\,\boldsymbol{C}^{-1}\,\frac{\partial \boldsymbol{\sigma}}{\partial t}\,p\,dx\,dz + \frac{d}{dt}\,\frac{1}{2}\int_{\mathbb{R}^2}\boldsymbol{\beta}^T\,\boldsymbol{C}^{-1}\,\boldsymbol{\beta}\,p^2\,dx\,dz.
\end{aligned} \tag{A.6}$$

We add (A.1) and the three first terms of (A.4). Using the symmetry of $\boldsymbol{C}$, there remains

$$\int_{\mathbb{R}^2}\rho_f\left({\boldsymbol{v}_s}^T\,\frac{\partial \boldsymbol{w}}{\partial t} + \boldsymbol{w}^T\,\frac{\partial \boldsymbol{v}_s}{\partial t}\right)dx\,dz = \frac{d}{dt}\,\frac{1}{2}\int_{\mathbb{R}^2} 2\,\rho_f\,{\boldsymbol{v}_s}^T\,\boldsymbol{w}. \tag{A.7}$$

Equations (19) and (A.1)-(A.7) yield

$$\frac{d}{dt}\,(E_1 + E_2) = -\int_{\mathbb{R}^2}\int_0^{\infty}\frac{\eta}{\pi\,\sqrt{\theta}}\,\boldsymbol{w}^T\,\mathrm{diag}\left(\frac{1}{\kappa_i\,\sqrt{\Omega_i}}\right)\boldsymbol{\psi}\,d\theta\,dx\,dz. \tag{A.8}$$

To calculate the right-hand side of (A.8), equation (21a) is multiplied by $\boldsymbol{w}^T$ or $\boldsymbol{\psi}^T$

$$\left\{\begin{array}{l}
\boldsymbol{w}^T\,\dfrac{\partial \boldsymbol{\psi}}{\partial t} - \boldsymbol{w}^T\,\dfrac{\partial \boldsymbol{w}}{\partial t} + \boldsymbol{w}^T\,\mathrm{diag}\,(\theta+\Omega_i)\;\boldsymbol{\psi} - \boldsymbol{w}^T\,\mathrm{diag}\,(\Omega_i)\;\boldsymbol{w} = \boldsymbol{0},\\
\boldsymbol{\psi}^T\,\dfrac{\partial \boldsymbol{\psi}}{\partial t} - \boldsymbol{\psi}^T\,\dfrac{\partial \boldsymbol{w}}{\partial t} + \boldsymbol{\psi}^T\,\mathrm{diag}\,(\theta+\Omega_i)\;\boldsymbol{\psi} - \boldsymbol{\psi}^T\,\mathrm{diag}\,(\Omega_i)\;\boldsymbol{w} = \boldsymbol{0}.
\end{array}\right. \tag{A.9}$$

Some algebraic operations on (A.9) yield

$$\begin{aligned}
\boldsymbol{\psi}^T\,\mathrm{diag}\,(\theta+2\,\Omega_i)\;\boldsymbol{w} = \;& \frac{\partial}{\partial t}\,\frac{1}{2}\,(\boldsymbol{w}-\boldsymbol{\psi})^T\,(\boldsymbol{w}-\boldsymbol{\psi})\\
& + \boldsymbol{\psi}^T\,\mathrm{diag}\,(\theta+\Omega_i)\;\boldsymbol{\psi} + \boldsymbol{w}^T\,\mathrm{diag}\,(\Omega_i)\;\boldsymbol{w}.
\end{aligned} \tag{A.10}$$

Injecting (A.10) in (A.8) leads to the relation (24)

$$\begin{aligned}
\frac{d}{dt}\,(E_1+E_2+E_3) = \;& -\int_{\mathbb{R}^2}\int_0^{\infty}\frac{\eta}{\pi\,\sqrt{\theta}}\left\{\boldsymbol{\psi}^T\,\mathrm{diag}\left(\frac{\theta+\Omega_i}{\kappa_i\,\sqrt{\Omega_i}\,(\theta+2\,\Omega_i)}\right)\boldsymbol{\psi}\right.\\
& \left. + \boldsymbol{w}^T\,\mathrm{diag}\left(\frac{\Omega_i}{\kappa_i\,\sqrt{\Omega_i}\,(\theta+2\,\Omega_i)}\right)\boldsymbol{w}\right\}\,d\theta\,dx\,dz.
\end{aligned} \tag{A.11}$$

It remains to prove that E (22) is a positive definite quadratic form. Concerning E_1, we write

$$\rho\, \boldsymbol{v_s}^T\, \boldsymbol{v_s} + \boldsymbol{w}^T\, \mathrm{diag}\,(\rho_{wi})\; \boldsymbol{w} + 2\,\rho_f\, \boldsymbol{v_s}^T\, \boldsymbol{w} = \boldsymbol{X_1}^T\; \boldsymbol{H_1}\, \boldsymbol{X_1} + \boldsymbol{X_3}^T\; \boldsymbol{H_3}\, \boldsymbol{X_3}, \tag{A.12}$$

where

$$\boldsymbol{X_i} = (v_{si}\; w_i)^T, \quad \boldsymbol{H_i} = \begin{pmatrix} \rho & \rho_f \\ \rho_f & \rho_{wi} \end{pmatrix}, \quad i = 1, 3. \tag{A.13}$$

Taking $\mathcal{S}_i$ and $\mathcal{P}_i$ to denote the sum and the product of the eigenvalues of matrix $\boldsymbol{H_i}$, we obtain

$$\begin{cases} \mathcal{P}_i = \det\, \boldsymbol{H_i} = \rho\,\rho_{wi} - \rho_f^2 = \chi_i > 0, \\ \mathcal{S}_i = \mathrm{tr}\, \boldsymbol{H_i} = \rho + \rho_w > 0. \end{cases} \tag{A.14}$$

The eigenvalues of $\boldsymbol{H_i}$ are therefore positive. This proves that E_1 is a positive definite quadratic form. The terms E_2, E_3 and $-\frac{dE}{dt}$ are obviously positive definite quadratic form because the involved matrices are definite positive. □

Appendix B. Matrices of propagation and dissipation

The matrices in (37) are

$$\boldsymbol{A} = \begin{pmatrix} \boldsymbol{0}_{4,4} & \boldsymbol{A}_1 & \boldsymbol{0}_{4,2N} \\ \boldsymbol{A}_2 & \boldsymbol{0}_{4,4} & \boldsymbol{0}_{4,2N} \\ \boldsymbol{0}_{2N,4} & \boldsymbol{A}_3 & \boldsymbol{0}_{2N,2N} \end{pmatrix}, \quad \boldsymbol{A}_3 = \begin{pmatrix} \dfrac{\rho_f}{\chi_1} & 0 & 0 & \dfrac{\rho}{\chi_1} \\ 0 & \dfrac{\rho_f}{\chi_3} & 0 & 0 \\ \vdots & \vdots & \vdots & \vdots \\ \dfrac{\rho_f}{\chi_1} & 0 & 0 & \dfrac{\rho}{\chi_1} \\ 0 & \dfrac{\rho_f}{\chi_3} & 0 & 0 \end{pmatrix}, \tag{B.1}$$

$$\boldsymbol{A}_1 = \begin{pmatrix} -\dfrac{\rho_{w1}}{\chi_1} & 0 & 0 & -\dfrac{\rho_f}{\chi_1} \\ 0 & -\dfrac{\rho_{w3}}{\chi_3} & 0 & 0 \\ \dfrac{\rho_f}{\chi_1} & 0 & 0 & \dfrac{\rho}{\chi_1} \\ 0 & \dfrac{\rho_f}{\chi_3} & 0 & 0 \end{pmatrix}, \quad \boldsymbol{A}_2 = \begin{pmatrix} -c_{11}^u & 0 & -\beta_1\, m & 0 \\ 0 & -c_{55}^u & 0 & 0 \\ -c_{13}^u & 0 & -\beta_3\, m & 0 \\ \beta_1\, m & 0 & m & 0 \end{pmatrix},$$

$$\boldsymbol{B} = \begin{pmatrix} \mathbf{0}_{4,4} & \boldsymbol{B}_1 & \mathbf{0}_{4,2N} \\ \boldsymbol{B}_2 & \mathbf{0}_{4,4} & \mathbf{0}_{4,2N} \\ \mathbf{0}_{2N,4} & \boldsymbol{B}_3 & \mathbf{0}_{2N,2N} \end{pmatrix}, \quad \boldsymbol{B}_3 = \begin{pmatrix} 0 & \dfrac{\rho_f}{\chi_1} & 0 & 0 \\ 0 & 0 & \dfrac{\rho_f}{\chi_3} & \dfrac{\rho}{\chi_3} \\ \vdots & \vdots & \vdots & \vdots \\ 0 & \dfrac{\rho_f}{\chi_1} & 0 & 0 \\ 0 & 0 & \dfrac{\rho_f}{\chi_3} & \dfrac{\rho}{\chi_3} \end{pmatrix}, \tag{B.2}$$

$$\boldsymbol{B}_1 = \begin{pmatrix} 0 & -\dfrac{\rho_{w1}}{\chi_1} & 0 & 0 \\ 0 & 0 & -\dfrac{\rho_{w3}}{\chi_3} & -\dfrac{\rho_f}{\chi_3} \\ 0 & \dfrac{\rho_f}{\chi_1} & 0 & 0 \\ 0 & 0 & \dfrac{\rho_f}{\chi_3} & \dfrac{\rho}{\chi_3} \end{pmatrix}, \quad \boldsymbol{B}_2 = \begin{pmatrix} 0 & -c^u_{13} & 0 & -\beta_1\, m \\ -c^u_{55} & 0 & 0 & 0 \\ 0 & -c^u_{33} & 0 & -\beta_3\, m \\ 0 & \beta_3\, m & 0 & m \end{pmatrix},$$

and $\boldsymbol{S}$ is the diffusive matrix

$$\boldsymbol{S} = \begin{pmatrix} \mathbf{0}_{4,4} & \mathbf{0}_{4,4} & \mathbf{S}_1 \\ \mathbf{0}_{4,4} & \mathbf{0}_{4,4} & \mathbf{0}_{4,2N} \\ \mathbf{S}_3 & \mathbf{0}_{2N,4} & \mathbf{S}_2 \end{pmatrix}, \quad \boldsymbol{S}_3 = \begin{pmatrix} 0 & 0 & -\Omega_1 & 0 \\ 0 & 0 & 0 & -\Omega_3 \\ \vdots & \vdots & \vdots & \vdots \\ 0 & 0 & -\Omega_1 & 0 \\ 0 & 0 & 0 & -\Omega_3 \end{pmatrix}, \tag{B.3}$$

$$\boldsymbol{S}_1 = \begin{pmatrix} -\dfrac{\rho_f}{\rho}\,\gamma_1\, a^1_1 & 0 & \cdots & -\dfrac{\rho_f}{\rho}\,\gamma_1\, a^1_N & 0 \\ 0 & -\dfrac{\rho_f}{\rho}\,\gamma_3\, a^3_1 & \cdots & 0 & -\dfrac{\rho_f}{\rho}\,\gamma_3\, a^3_N \\ \gamma_1\, a^1_1 & 0 & \cdots & \gamma_1\, a^1_N & 0 \\ 0 & \gamma_3\, a^3_1 & \cdots & 0 & \gamma_3\, a^3_N \end{pmatrix},$$

$$\boldsymbol{S}_2 = \begin{pmatrix} \gamma_1\, a^1_1 + (\theta^1_1 + \Omega_1) & 0 & \cdots & \gamma_1\, a^1_N & 0 \\ 0 & \gamma_3\, a^3_1 + (\theta^3_1 + \Omega_3) & \cdots & 0 & \gamma_3\, a^3_N \\ \vdots & \vdots & \vdots & \vdots & \vdots \\ \gamma_1\, a^1_1 & 0 & \cdots & \gamma_1\, a^1_N + (\theta^1_N + \Omega_1) & 0 \\ 0 & \gamma_3\, a^3_1 & \cdots & 0 & \gamma_3\, a^3_N + (\theta^3_N + \Omega_3) \end{pmatrix}.$$

Appendix C. Proof of proposition 4

We denote $\boldsymbol{P}_{\mathscr{B}}$ the change-of-basis matrix satisfying

$$\boldsymbol{U} = \boldsymbol{P}_{\mathscr{B}} \, (\boldsymbol{U}_1 \, , \boldsymbol{U}_3 \, , \boldsymbol{\sigma} \, , \, p)^T \, , \tag{C.1}$$

with

$$\boldsymbol{U}_i = (v_{si} \, , \, w_i \, , \, \psi_1^i \, , \, \cdots \, , \, \psi_N^i)^T, \quad i = 1, 3. \tag{C.2}$$

The matrix $\boldsymbol{P}_{\mathscr{B}}$ is thus invertible, and the matrices $\boldsymbol{S}$ (Appendix B) and $\boldsymbol{S}_{\mathscr{B}} = \boldsymbol{P}_{\mathscr{B}}^{-1} \, \boldsymbol{S} \boldsymbol{P}_{\mathscr{B}}$ are similar. The matrix $\boldsymbol{S}_{\mathscr{B}}$ writes

$$\boldsymbol{S}_{\mathscr{B}} = \begin{pmatrix} \tilde{\boldsymbol{S}}_1 & \boldsymbol{0}_{N+2,N+2} & \boldsymbol{0}_{N+2,3} & \boldsymbol{0}_{N+2,1} \\ \boldsymbol{0}_{N+2,N+2} & \tilde{\boldsymbol{S}}_3 & \boldsymbol{0}_{N+2,3} & \boldsymbol{0}_{N+2,1} \\ \boldsymbol{0}_{3,N+2} & \boldsymbol{0}_{3,N+2} & \boldsymbol{0}_{3,3} & \boldsymbol{0}_{3,1} \\ \boldsymbol{0}_{1,N+2} & \boldsymbol{0}_{1,N+2} & \boldsymbol{0}_{1,3} & 0 \end{pmatrix} \tag{C.3}$$

with $(i = 1, 3)$

$$\tilde{\boldsymbol{S}}_i = \left(\begin{array}{cc|cccc} 0 & 0 & -\dfrac{\rho_f}{\rho} \, \gamma_i \, a_1^i & -\dfrac{\rho_f}{\rho} \, \gamma_i \, a_2^i & \cdots & -\dfrac{\rho_f}{\rho} \, \gamma_i \, a_N^i \\ 0 & 0 & \gamma_i \, a_1^i & \gamma_i \, a_2^i & \cdots & \gamma_i \, a_N^i \\ \hline 0 & -\Omega_i & \gamma_i \, a_1^i + (\theta_1^i + \Omega_i) & \gamma_1 \, a_2^i & \cdots & \gamma_i \, a_N^i \\ 0 & -\Omega_i & \gamma_i \, a_1^i & \gamma_i \, a_2^i + (\theta_2^i + \Omega_i) & \cdots & \gamma_i \, a_N^i \\ \vdots & \vdots & \vdots & \vdots & \vdots & \vdots \\ 0 & -\Omega_i & \gamma_i \, a_1^i & \gamma_i \, a_2^i & \cdots & \gamma_i \, a_N^i + (\theta_N^i + \Omega_i) \end{array} \right). \tag{C.4}$$

The characteristic polynomial of $\boldsymbol{S}$ is

$$P_{\boldsymbol{S}}(s) = s^4 \, P_{\tilde{\boldsymbol{S}}_1}(s) \, P_{\tilde{\boldsymbol{S}}_3}(s), \tag{C.5}$$

where $P_{\tilde{\boldsymbol{S}}_i}(s)$ denotes the characteristic polynomial of the matrix $\tilde{\boldsymbol{S}}_i$, i.e. $\tilde{\boldsymbol{S}}_i(s) = \det(\tilde{\boldsymbol{S}}_i - s \, \boldsymbol{I}_{N+2})$ with $\boldsymbol{I}_{N+2}$ the $(N + 2)$-identity matrix. This $(N + 2)$-determinant is expanded along the first column. The line I and the column J of the $(N + 1)$-determinant thus obtained are denoted L_I and C_J, respectively $(0 \leqslant I, J \leqslant N)$. The following algebraic manipulations are then performed successively:

$$\begin{aligned} &(i) \quad L_\ell \leftarrow L_\ell - L_0, \quad \ell = 1, \cdots, N, \\ &(ii) \quad C_0 \leftarrow C_0 \, \prod_{\ell=1}^{N} (\theta_\ell^i + \Omega_i - s), \\ &(iii) \quad C_0 \leftarrow C_0 - (s - \Omega_1) \, \prod_{\substack{k=1 \\ k \neq \ell}}^{N} (\theta_k^i + \Omega_i - s) \, C_\ell, \quad \ell = 1, \cdots, N. \end{aligned} \tag{C.6}$$

One deduces

$$P_{\tilde{\boldsymbol{S}}_i}(s) = -s\,Q_i(s) = s^2 \prod_{\ell=1}^{N} (\theta^i_\ell + \Omega_i - s) + \gamma_i\, s\,(s - \Omega_i) \sum_{\ell=1}^{N} a^i_\ell \prod_{\substack{k=1\\k\neq\ell}}^{N} (\theta^i_k + \Omega_i - s). \tag{C.7}$$

From equation (C.7), one has $P_{\tilde{\boldsymbol{S}}_i}(0) \neq 0$ while $Q_i(0) \neq 0$, therefore 0 is an eigenvalue of the matrix $\tilde{\boldsymbol{S}}_i$ with multiplicity 1. In what follows, the positivity of the coefficients θ^i_ℓ, a^i_ℓ of the diffusive approximation is used. In the limit $s \to 0^+$, then asymptotically

$$P_{\tilde{\boldsymbol{S}}_i}(s) \underset{s\to 0^+}{\sim} -\gamma_i\, \Omega_i\, s \sum_{\ell=1}^{N} a^i_\ell \prod_{\substack{k=1\\k\neq\ell}}^{N} (\theta^i_k + \Omega_i) \Rightarrow \operatorname{sgn}\left(P_{\tilde{\boldsymbol{S}}_i}(0^+)\right) = -1. \tag{C.8}$$

Moreover, using (43), then at the quadrature abscissae one has for all $\ell = 1, \cdots, N$

$$P_{\tilde{\boldsymbol{S}}_i}(\theta^i_\ell + \Omega_i) = \gamma_i\, \theta^i_\ell\, (\theta^i_\ell + \Omega_i)\, a^i_\ell \prod_{\substack{k=1\\k\neq\ell}}^{N} (\theta^i_k - \theta^i_\ell) \Rightarrow \operatorname{sgn}\left(P_{\tilde{\boldsymbol{S}}_i}(\theta^i_\ell + \Omega_i)\right) = (-1)^{\ell+1}. \tag{C.9}$$

Finally, the following limit holds

$$P_{\tilde{\boldsymbol{S}}_i}(s) \underset{s\to +\infty}{\sim} (-1)^N\, s^{N+2} \Rightarrow \operatorname{sgn}\left(P_{\tilde{\boldsymbol{S}}_i}(+\infty)\right) = (-1)^N. \tag{C.10}$$

We introduce the following intervals

$$I^i_N =]\theta^i_N + \Omega_i, +\infty[,\ I^i_\ell =]\theta^i_\ell, \theta^i_{\ell+1} + \Omega_i],\ \text{for}\ \ell = 1, \cdots, N-1,\ I^i_0 =]0, \theta^i_1 + \Omega_i]. \tag{C.11}$$

The real-valued continuous function $P_{\tilde{\boldsymbol{S}}_i}$ changes of sign on each interval I^i_ℓ. Consequently, according to the intermediate value theorem, $P_{\tilde{\boldsymbol{S}}_i}$ has at least one zero in each interval. Since $P_{\tilde{\boldsymbol{S}}_i}$ has at the most $N+1$ distinct zeros in $]0, +\infty[$, we deduce that $\exists\,!\ s^i_\ell \in I^i_\ell / P_{\tilde{\boldsymbol{S}}_i}(s^i_\ell) = 0, \quad \ell = 1, \cdots, N+1$. Using equation (C.5), the characteristic polynomial of $\boldsymbol{S}$ (C.7) is therefore

$$P_{\boldsymbol{S}}(s) = s^6 \prod_{\ell=1}^{N+1} (s - s^1_\ell)\,(s - s^3_\ell), \tag{C.12}$$

which concludes the proof. □

References

[1] M. A. Biot, Theory of propagation of elastic waves in a fluid-saturated porous solid. I: Low-frequency range, J. Acoust. Soc. Am. 28 (2) (1956) 168–178.

[2] T. Bourbié, O. Coussy, B. Zinszner, Acoustics of Porous Media, Gulf Publishing Company, Houston, 1987.

[3] J. M. Carcione, Wave Fiels in real Media: Wave Propagation in Anisotropic, Anelastic, Porous and Electromagnetic Media, 2nd Edition, Elsevier, Amsterdam, 2007.

[4] R. F. Gibson, Principles of Composite Material Mechanics, McGraw-Hill, New York, 1989.

[5] D. S. Chandrasekharaiah, S. C. Cowin, A complete solution for a unified system of field equations of thermoelasticity and poroelasticity, Acta Mech. 99 (1993) 225–233.

[6] M. A. Biot, Theory of propagation of elastic waves in a fluid-saturated porous solid. II: High-frequency range, J. Acoust. Soc. Am. 28 (2) (1956) 179–191.

[7] T. J. Plona, Observation of a second bulk compressional wave in a porous medium at ultrasonic frequencies, App. Phys. Lett. 36 (4) (1980) 259–261.

[8] D. L. Johnson, J. Koplik, R. Dashen, Theory of dynamic permeability and tortuosity in fluid-saturated porous media, J. Fluid Mech. 176 (1987) 379–402.

[9] C. Lubich, Discretized fractional calculus, SIAM J. Math. Anal. 17 (1986) 704–719.

[10] J. M. Carcione, C. Morency, J. E. Santos, Computational poroelasticity - a review, Geophysics 75 (5) (2010) 75A229–75A243.

[11] G. Chiavassa, B. Lombard, Time domain numerical modeling of wave propagation in 2D heterogeneous porous media, J. Comput. Phys. 230 (2011) 5288–5309.

[12] Y. J. Masson, S. R. Pride, Finite-difference modeling of Biot's poroelastic equations across all frequencies, Geophysics 75 (2) (2010) N33–N41.

[13] J. F. Lu, A. Hanyga, Wave field simulation for heterogeneous porous media with singular memory drag force, J. Comput. Phys. 208 (2) (2005) 651–674.

[14] H. Haddar, J. R. Li, D. Matignon, Efficient solution of a wave equation with fractional-order dissipative terms, J. Comput. Appl. Math. 234 (6) (2010) 2003–2010.

[15] L. Yuan, O. P. Agrawal, A numerical scheme for dynamic systems containing fractional derivatives, J. Vib. Acoust. 124 (2) (2002) 321–324.

[16] K. Diethelm, An investigation of some nonclassical methods for the numerical approximation of caputo-type fractional derivatives, Numer. Algor. 47 (2008) 361–390.

[17] C. Birk, C. Song, An improved non-classical method for the solution of fractional differential equations, Comput. Mech. 46 (2010) 721–734.

[18] J. M. Carcione, Wave propagation in anistropic, saturated porous media: Plane-wave theory and numerical simulation, J. Acoust. Soc. Am. 99 (5) (1996) 2655–2666.

[19] G. I. Lemoine, M. Y. Ou, R. J. LeVeque, High-resolution finite volume modeling of wave propagation in orthotropic poroelastic media, SIAM J. Sci. Comput. 35 (1) (2013) B176–B206.

[20] A. Hanyga, J. F. Lu, Wave field simulation for heterogeneous transversely isotropic porous media with the JKD dynamic permeability, Comput. Mech. 36 (2005) 196–208.

[21] G. Chiavassa, B. Lombard, J. Piraux, Numerical modeling of 1D transient poroelastic waves in the low-frequency range, J. Comput. Appl. Math. 234 (2010) 1757–1765.

[22] G. Chiavassa, B. Lombard, Wave propagation across acoustic / Biots media: a finite-difference method, Commun. Comput. Phys. 13 (4) (2013) 985–1012.

[23] E. Blanc, G. Chiavassa, B. Lombard, Biot-JKD model: Simulation of 1D transient poroelastic waves with fractional derivatives, J. Comput. Phys. 237 (2013) 1–20.

[24] E. Blanc, G. Chiavassa, B. Lombard, A time-domain numerical modeling of two-dimensional wave propagation in porous media with frequency-dependent dynamic permeability, J. Acoust. Soc. Am. 134 (6) (2013) 4610–4623.

[25] M. A. Biot, Generalized theory of acoustic propagation in porous dissipative media, J. Acoust. Soc. Am. 34 (5) (1962) 1254–1264.

[26] O. Coussy, Mechanics of Porous Continua, 2nd Edition, John Wiley and Sons, New York, 1995.

[27] J. R. Rice, M. P. Cleary, Some basic stress diffusion solutions for fluid-saturated elastic porous media with compressible constituents, Rev. Geophysics 14 (2) (1976) 227–241.

[28] F. Dubois, A. Galucio, N. Point, Introduction à la dérivation fractionnaire : théorie et applications, `http://www.math.u-psud.fr/ fdubois` (2010).

[29] A. N. Norris, On the viscodynamic operator in Biot's equations of poroelasticity, J. Wave-Material Interaction 1 (4) (1986) 365–380.

[30] R. N. Chandler, D. L. Johnson, The equivalence of quasi-static flow in fluid-saturated porous media and Biot's slow wave in the limit of zero frequency, J. Appl. Phys. 52 (1981) 3391–3395.

[31] J. M. Carcione, F. Cavallini, Energy balance and fundamental relations in anisotropic-viscoelastic media, Wave Motion 18 (1) (1993) 11–20.

[32] B. P. Flannery, W. H. Press, S. A. Teukolsky, W. T. Vetterling, Numerical Recipes in C: the Art of Scientific Computing, 2nd Edition, Cambridge University Press, Cambridge, 1992.

[33] F. Kappel, A. Kuntsevich, An implementation of Shor's r-algorithm, Comput. Optim. Appl. 15 (2) (2000) 193–205.

[34] N. Z. Shor, Minimization Methods for Non-Differentiable Functions, Springer-Verlag, Berlin, 1985, springer Series in Computational Mathematics, vol. 3.

[35] A. Rekik, R. Brenner, Optimization of the collocation inversion method for the linear viscoelastic homogenization, Mech. Res. Commun. 38 (2011) 305–308.

[36] R. J. LeVeque, Finite Volume Methods for Hyperbolic Problems, Cambridge University Press, Cambridge, 2002.

[37] T. Schwartzkopff, M. Dumbser, C. Munz, Fast high-order ADER schemes for linear hyperbolic equations, J. Com-

put. Phys. 197 (2) (2004) 532–539.

[38] J. C. Strikwerda, Finite Difference Schemes and Partial Differential Equations, 2nd Edition, Chapman & Hall, London, 1999.

[39] C. B. Moller, C. F. Loan, Nineteen dubious ways to compute the exponential of a matrix, twenty-five years later, SIAM Rev. 45 (2003) 3–49.

[40] B. Gurevich, M. Schoenberg, Interfaces conditions for Biot's equations of poroelasticity, J. Acoust. Soc. Am. 105 (1999) 2585–2589.

[41] R. J. LeVeque, C. Zhang, The immersed interface method for wave equations with discontinuous coefficients, Wave Motion 25 (1997) 237–263.

[42] Z. Li, R. J. LeVeque, The immersed interface method for elliptic equations with discontinuous coefficients and singular sources, SIAM J. Num. Anal. 31 (1994) 1019–1044.

[43] N. Dai, A. Vafidis, E. R. Kanasewich, Wave propagation in heterogeneous porous media: a velocity-stress, finite-difference method, Geophysics 60 (2) (1995) 327–340.

[44] G. A. McMechan, M. J. Yedlin, Analysis of dispersive waves by wave field transformation, Geophysics 46 (6) (1981) 869–874.

[45] T. A. Mokhtar, R. B. Herrmann, D. R. Russell, Seismic velocity and Q model for the shallow structure of the Arabian shield from short-period Rayleigh waves, Geophysics 53 (11) (1988) 1379–1387.

[46] P. C. Waterman, R. Truell, Multiple scattering of waves, J. Math. Phys. 4 (1961) 512–537.

[47] M. Chekroun, L. Le Marrec, B. Lombard, J. Piraux, Time-domain numerical simulations of multiple scattering to extract elastic effective wavenumbers, Waves Random Complex Media 22 (2012) 398–422.

[48] J. M. Conoir, A. Norris, Effective wavenumbers and reflection coefficients for an elastic medium containing random configurations of cylindrical scatterers, Wave Motion 47 (2010) 183–197.

[49] V. Tournat, V. Pagneux, D. Lafarge, L. Jaouen, Multiple scattering of acoustic waves and porous absorbing media, Phys. rev. E 70 (2) (2004) 026609.

[50] F. Luppé, J. M. Conoir, S. Robert, Coherent waves in a multiply scattering poro-elastic medium obeying Biot's theory, Waves Random Complex Media 18 (2008) 241–254.

[51] D. Lafarge, P. Lemarinier, J. F. Allard, V. Tarnow, Dynamic compressibility of air in porous structures at audible frequencies, J. Acoust. Soc. Am. 102 (4) (1997) 1995–2005.

[52] N. Nemati, Macroscopic theory of sound propagation in rigid-framed porous materials allowing for spatial dispersion: principle and validation, Ph.D. thesis, Université du Maine, France (2012).

[53] F. Liu, V. Anh, I. Turner, Numerical solution of the space fractional Fokker-Planck equation, J. Comput. Appl. Math. 166 (2004) 209–219.

[54] C. Tadjeran, M. M. Meerschaert, H. P. Scheffler, A second-order accurate numerical approximation for the fractional diffusion equation, J. Comput. Phys. 213 (2006) 205–213.